40
Theoretical Tool Box for a Better Catalytic Understanding

Michel Waroquier, Kristof De Wispelaere, Julianna Hajek, Sven Rogge, Jeroen Van Der Mynsbrugge, and Veronique Van Speybroeck

Ghent University, Center for Molecular Modeling, Technologiepark 903, 9052 Zwijnaarde, Belgium

40.1
Introduction

Theoretical modeling has nowadays taken an indispensable role in many fields of science and engineering, thanks to the availability of systematically stronger computing power and the steady development of new ingenious theoretical methods and numerical implementations. Within the field of catalysis, modeling has also taken a prominent role. A lot of experimental papers are combined with computational modeling to explore issues such as the nature of the active site, the determination of reaction rates at the single reaction level, and so on. These are typically questions that are very hard to assess purely from experimental point of view. Theory can thus be used to explain and rationalize experimentally observed features. However, the field has evolved substantially and theory has now come to a point where it can even be used in a predictive manner. Nice examples are high-throughput screening studies, where a large database of hypothetical materials is screened for desirable properties. Seminal studies of this kind were published by Joos *et al.* [1], Kim *et al.* [2], Simon *et al.* [3], and Colon and Snurr [4]. Such efforts may lead to the design of dedicated experiments on a set of promising materials. Ideally, theory could answer important questions related to the activity, selectivity, and stability of the catalyst. However, one must be realistic, despite the enormous progress made during the last decades, computational catalyst design still needs to overcome many hurdles in order to be used as an all-in toolbox. Many issues are related to the typical length and time scales encountered in a catalytic process. The overall function of a catalyst is the interplay between many multiscale phenomena both in space and time. This was nicely illustrated by Weckhuysen in his review on spatial heterogeneities in catalytic solids [5]. In this chapter we give our view on the question whether we dispose anno 2016 of a theoretical toolbox for a better catalytic understanding.

Nanotechnology in Catalysis: Applications in the Chemical Industry, Energy Development, and Environment Protection, First Edition. Edited by Bert Sels and Marcel Van de Voorde.

To answer these questions, one must also define its expectations. Until recently, the catalytic community was satisfied if theory succeeded in suggesting some plausible reaction schemes and could reproduce qualitatively experimental findings. However, with the rapid evolution of the field, the expectations have currently taken a whole other dimension. Nowadays, methods are developed and explored to reach chemical and kinetic accuracy for reaction enthalpies and rate constants [6–8]. In some cases this has proven to be achievable, but at the expense of a serious computational cost, which hampers their applicability as mainstream methodologies. Furthermore, such reliable theoretical predictions also request the availability of very accurate experimental data. For example, to predict reaction rates with kinetic accuracy – that is, within a factor 10 from the experiment – one needs to dispose of experimental data that provide the chemical kinetics for a single reaction within an often very complex reaction network. Thus, the development of such accurate methods also imposes challenges for the experimentalists to generate data that are comparable with the produced theoretical data.

Next, the catalyst should be studied at work, thus at operating conditions [9]. This imposes a huge challenge for theory, as this requires models that account for realistic process conditions involving actual reaction temperatures, pressures, loading of the guest species, and other degrees of freedom. One can imagine that in these circumstances the catalytic process becomes very complex and one cannot resort anymore to the textbook concept of a single transition state and a restricted number of configurations on the potential energy surface. Very recently, new methods are being explored within the field of computational catalysis, such as enhanced molecular dynamics (MD) methods that allow sampling the free energy surface at operating conditions [10–23]. However, this field is in full exploration and new methodologies are being developed to apply advanced molecular dynamics techniques in the field of catalysis.

In this chapter we will focus on heterogeneous catalysis and in particular on catalytic reactions taking place in the pores of a nanoporous material. Due to the heterogeneous character of the chemical process the complexity of the reaction also increases. Such applications are a good value indicator to assess the available toolbox of techniques and algorithms. We will concentrate on catalytic reactions taking place in two types of nanoporous materials: zeolites and metal-organic frameworks (MOFs). Zeolites are crystalline framework-structured aluminosilicates with pores and cages of molecular dimensions (<2 nm). Their characteristic pore dimensions, high surface area, porosity, diversity, and so on, make them very tractable in a wide scope of applications [24] making zeolites the workhorses of today's chemical industry. MOFs are hybrid nanoporous materials build from inorganic moieties connected with organic linkers (Figure 40.1). These last materials have a more recent history and their probable catalytic potential is still under exploration. This class of new materials knows a still increasing interest from the community due to its building block concept resulting to a tunable composition and structural diversity combined with a high porosity. These properties lead to a broad variety of applications varying from

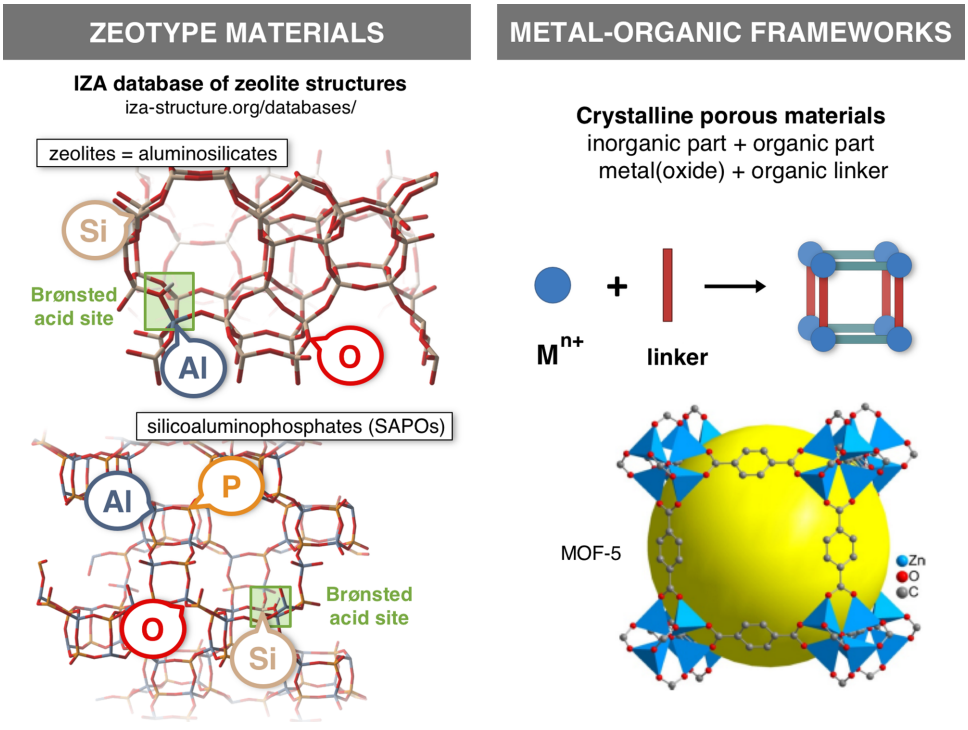

Figure 40.1 Schematic of the versatility of nanoporous materials. By combining different building blocks a wide variety of zeotype materials and metal-organic frameworks can be synthesized. (Adapted with permission from Ref. [28]. Copyright 1999, Nature Publishing Group.)

adsorption and gas storage, separation, and optics and sensing to catalysis [25–27]. Today, it is too premature to predict the future of MOFs as industrial catalysts, but together with other properties that are further evolved in the context of valorization, one needs a proper description of the metal sites and their accessibility by guest molecules.

The computational toolbox, which is available nowadays – with its strengths and limitations – can certainly not be used as a black box. Even though a lot of programs are currently available for a large community, computational catalysis requires the knowledge of an advanced user, who masters the strengths and the weaknesses of current computational methods. The whole modeling procedure consists of various steps, and each merits special attention to reach the final objective of an optimal tool to describe heterogeneous catalysis in all its complexity.

A good modeling trajectory should fulfill many criteria and should cover many features. First, it is essential to model the catalyst's active site by fully taking into account the effects of the molecular environment. Next, the adsorption of the reactants at the active site and the reaction itself should be studied. The latter encompasses the determination of the transition state(s), calculation of the

reaction rate constant, and identification of the various factors governing the reaction rate.

In this contribution, focus lies on the adequacy of contemporary state-of-the-art techniques present in the current toolbox to achieve the highest reliability, reproducibility, and accuracy in the description of catalytic reactions in the pores of a nanoporous material. We realize that this is a rapidly varying and steadily progressing issue, but for any reader such an overview, reporting the good performing features, the issues that are subject to improvement and some critical notes of present modeling tools, remains very instructive. Some similar exercise has been presented by Sauer and Freund [9] discussing the hierarchy of model studies on catalytic reactions with increasing complexity.

We will focus on some particular items that took our attention starting from our own expertise in modeling heterogeneous catalysis. It encompasses the models to describe the catalytic site including all ingredients that could have a significant effect on the reaction. This contribution also tries to discuss carefully the advantages/disadvantages of static approaches versus dynamic models. Modeling of a reaction always starts from a reactive complex, but the construction of such a complex requires a lot of attention as it determines for a large part the initial stages of the reaction path on the free energy surface. A special section is devoted on the determination of chemical kinetics of the catalytic reaction and thus identification of the transition state (TS) or transition state region that constitutes one of the major objectives of a modeling toolbox. Finally, computational spectroscopy has reached such a level of accuracy that it assists in interpreting *in situ* spectroscopic measurements that are indispensable for characterization of reaction intermediates.

40.2 Modeling the Catalytic Active Site

40.2.1 Taking Into Account Topology

An important issue when modeling catalytic processes in nanoporous materials is to select an appropriate model to simulate the extended molecular environment of the host material itself. We first illustrate this point for zeolites. Zeolites are bulky materials with a large amount of atoms and thus computationally accurate methods need to be used to account for a representative fraction of the material within a reasonable computational time. The first attempts over the years to model the active site in a zeolite framework are based on small clusters containing a limited number of tetrahedral atoms (illustrated by a 1 T and 5 T cluster in Figure 40.2a and b). The main advantage of such small clusters is their limited number of atoms, which allowed usage of very accurate electronic structure methods for the calculation of the energy of the system. Although they have shown their practical use in times where computational resources were rather

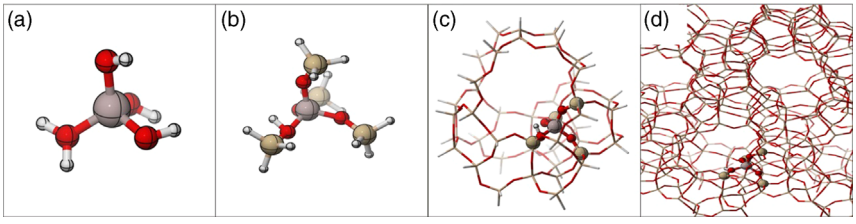

Figure 40.2 Illustration of various models to account for the zeolite topology: a 1 T cluster (a), a 5 T cluster (b), a 46 T cluster for H-ZSM-5 (c), and the periodic structure of H-ZSM-5 (d) with indication of the acid site. (Adapted with permission from Ref. [23]. Copyright 2014, The Royal Society of Chemistry.)

limited by giving some valuable qualitative insight, they are no longer of any use in current models as the topology is completely neglected. In a next generation, more extended clusters are considered. A finite cluster is cut from the periodic structure of the material that needs to be sufficiently large to account properly for the topology. Figure 40.2c shows a finite cluster model (46 T) corresponding to the MFI topology. Typically, such clusters are terminated by hydrogen atoms that are fixed in space to prevent the unphysical collapse of the cluster during geometry optimization. This of course leads to the drawback that the flexibility of the nanoporous material is not fully exploited. Another shortcoming is that extended clusters containing many atoms become computationally hard to manage with very accurate quantum chemical methods. To prevent this computational bottleneck, multilayer approaches such as ONIOM and other QM/MM methods were introduced [8,21,29–34]. The ONIOM method was used in the work of Maihom *et al.* [29] to model reactions in H-ZSM-5. These authors considered a 128 T cluster, in which only 12 T atoms were treated at the DFT level for reasons of computational efficiency. The rest of the cluster was modeled using the universal force field (UFF) and during the geometry optimization only a small portion of the cluster was relaxed. To mimic the electrostatic effect of the remainder of the infinite zeolite lattice, the clusters were further embedded in a set of point charges to reproduce the zeolite Madelung potential.

In addition, the accuracy of all these QM/MM schemes largely depends on the cluster size, the QM method – for density functional theory (DFT) more specifically the exchange-correlation functional – and the basis set, as pointed out by Bell and coworkers [32]. Therefore, use of cluster models requires a thorough benchmark for each system and for each property of interest. In any case, cluster models give a rather limited view of the material, since flexibility is not accounted for.

A still valid and interesting advantage of cluster models is that numerical algorithms to search for transition states are better developed than in solid-state codes, which are typically used for periodic representations of the crystal lattice. A procedure that is often used to remedy this issue is to localize a transition state in a cluster model and transfer it afterwards to a periodic model. As such

good initial guesses for transition states in periodic models are obtained, which may help to localize the transition state in the periodic model.

Alternatively, the nanoporous material can be best represented by a periodic model. In such periodic representation of a nanoporous material, one or more unit cells of the framework are included in the model. Figure 40.2d displays a periodic model of the well-known MFI material. Use of periodic models to mimic the periodic structure of the material is by definition the most appropriate way to simulate the active site, as all ingredients characterizing the active site such as its location in the pores of the nanoporous material, the shape of the pores and channels, flexibility of the frame, and so on, are taken into account in a natural way. Periodic calculations of framework materials are typically conducted with codes that find their origin in solid-state applications.

Both in cluster and periodic-based models, density functional theory is the method of choice to treat the systems of interest, thanks to their favorable balance between accuracy and computational efficiency. For periodic-based calculations, the so called gradient corrected functionals are still frequently used as they have proven their merits for true solid-state systems. Use of hybrid functionals or more advanced functionals (metahybrid functionals, etc) is currently implemented in most of the periodic codes (VASP, CRYSTAL, etc) but still very demanding for geometry optimizations of the periodic cell and thus not systematically applied.

As long-range electron–electron interactions are not involved in commonly applied local-density functionals they have to be inserted separately. In most of the cases Grimme D3 dispersion corrections were used [35].

It is not the intention to give a full overview of all electronic structure methods currently available, as this would entail a review on its own. However, we refer to some dedicated reviews and other interesting references on the topic [23,36].

40.2.2 Determining the Nature of the Active Site

One of the challenges in modeling catalysis in nanoporous materials consists in determining the nature of the active site. Catalysis in zeolites takes place in the surroundings of an active site such as a Brønsted acidic center originating from a charge-compensating proton at an aluminum substitutional defect in the zeolite framework or at an extra-framework Lewis acid site. Metal-exchanged zeolites received considerable attention in catalysis. Some examples are the Cu-SSZ-13 material, which have been studied for processes such as the ammonia-assisted selective catalytic reduction (NH_3-SCR) of NO_x or Ti-substituted zeolites, which proved to be effective and versatile partial oxidation catalysts [37]. These are only a limited number of examples from the wealth of literature available on the topic. For more detailed discussions, we refer to one of our recent reviews [36]. There we pointed out that for these metal-exchanged zeolites, it is very complex to elucidate the true nature of the active site and we demonstrated the added

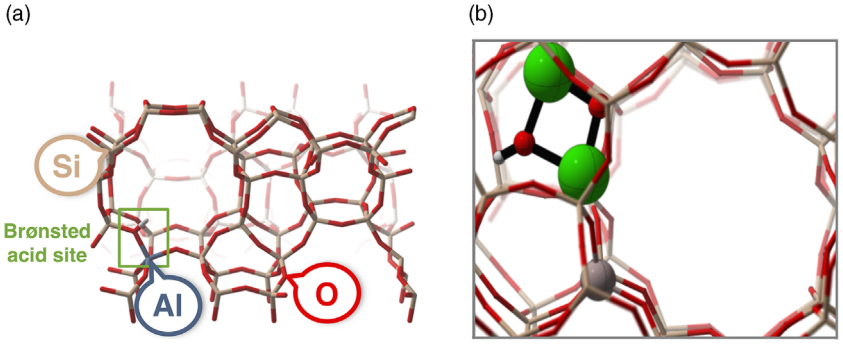

Figure 40.3 Brønsted acid site (BAS) in H-ZSM-5 with an Al substitution and the charge compensating proton (a); Lewis acidic site by the presence of charge compensating Ca cation. After modification with Ca, ZSM-5 can contain $CaOCaOH^+$ species at the Al substitution. (Adapted with permission from Ref. [38]. Copyright 2016, permission from Wiley-VCH Verlag GmbH.)

value of modeling to resolve these issues. Within this chapter we will focus on examples taken from Brønsted acidic zeolite catalysis. Figure 40.3 shows a schematic representation of a zeolite model in which a Brønsted acidic site is incorporated and a Lewis acidic site is present.

Modeling of the active site is not that trivial as could be expected at first sight. There are also some challenging issues that have to be taken into account. In most modeling studies on Brønsted acidic zeolites, one acid site is taken into consideration in the molecular model. A first question concerns the position of this acid site. Aluminum siting in zeolite materials is a fairly complex problem in itself; for example, for H-ZSM-5, the distribution of aluminum has been shown to depend mainly on the method and conditions that are applied for the synthesis of the catalyst [39–41]. As a result, the selection of a single active site remains somewhat ambiguous. In many cases, more pragmatic choices are made. A reasonable selection consists in retaining only those aluminum substitutions that give rise to acid sites that are accessible to the reactant and thus for which enough space is available to host the various transition states. In case of the H-ZSM-5 material, one often positions the acidic site at the T12 position, located at the intersection of the straight and sinusoidal channels as this position ensures enough place for the reactions to take place. Furthermore, once the aluminum is placed in the framework, one could select the bridging hydroxyl groups with highest acid strength or with lowest deprotonation energy. This approach has frequently been used in literature [7,42,43].

Another factor that complicates the accurate description of the active site is the presence of high loadings of protic molecules in the surroundings of a Brønsted acid site. It has been found that sufficient amounts of water or methanol molecules are able to deprotonate a zeolite's Brønsted acid site at operating

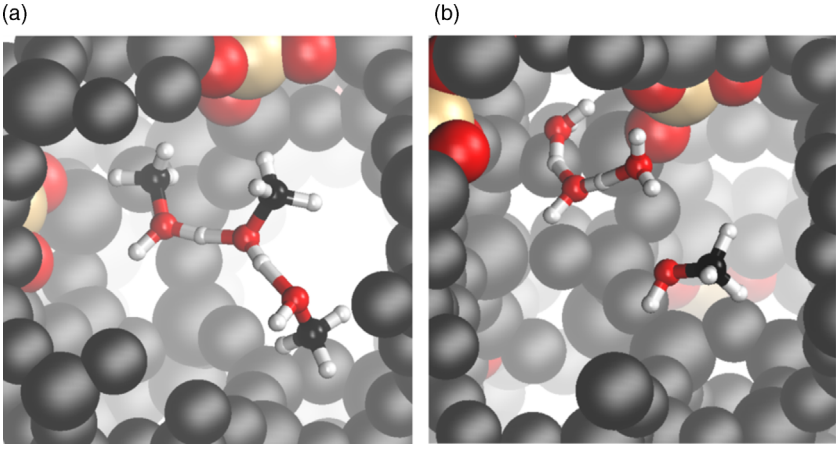

Figure 40.4 Protonated methanol (a) and water (b) cluster occupying a Brønsted acid site of H-SAPO-34 at 330 °C and around ambient pressure.

conditions with the formation of protonated water or methanol clusters as depicted in Figure 40.4 [11–14,44–52]. These protonated clusters might in turn initiate reaction; however, such clusters exhibit a distinct intrinsic reactivity (*vide infra*). Such effects can be studied with advanced molecular dynamics techniques as described further in this chapter.

Determining the nature of the active site within MOFs has proven a true challenge as in many materials catalytic active sites are created by intentional creation of defects. These defects do increase the accessibility of the active sites, which in most cases represent Lewis acid centers formed by the metals of the MOF. From a molecular modeling point of view, we must also need to explore the advantage and the usefulness of the active site in the course of the reaction under study. We illustrate this concept for some Lewis-catalyzed reactions in MOFs and more in particular for the UiO-66 type of material consisting of $Zr_6O_4(OH)_4$ inorganic building blocks and terephthalate linkers. This Zr(IV)-based MOF received considerable attention [53–55], as the UiO-66 material possesses a high thermal and chemical stability. Windows with a diameter of about 6 Å guarantee the accessibility to the cages. For Lewis-catalyzed reactions it was demonstrated that terephthalate defects are responsible for the catalytic activity in UiO-66 [27,56]. Moreover, catalytic performance could in many cases be improved by functionalization of the linkers. It is a challenge for the theory whether the current techniques in the current toolbox succeed in reproducing the catalytic activity as measured in diverse experiments.

Most of the experimental investigations on catalytic performance of MOFs are concentrated on oxidation reactions [27] and other reactions like the citronellal cyclization [57] where the catalytic activity is concentrated around the metal, which acts as a Lewis acid site.

Defect sites can be created by linker deficiencies increasing the Lewis acid strength and making the metal center more accessible for potential reactant molecules. Determining the structure of the defect site or active site has proven a true challenge both for experimentalists and theoreticians, as the type of a deficiency in UiO-66 can be very broad varying from a missing linker to a missing Zr brick [58]. Removal of a benzenedicarboxylate (BDC) linker requires a charge balancing species. By means of single crystal X-ray diffraction (SXRD), the presence of two hydroxyl group terminations and/or coordinating water molecules has been observed [59,60]. Trickett *et al.* postulated the presence of an extra hydroxide anion per defect site, bringing the total amount of defect coordinating water units on three. Recently, a variety of theoretical studies appeared that are based both on static and molecular dynamics first principle calculations both on clusters and on periodic models to unravel the nature of the active site and the coordination of water to the defect sites [61,62].

Catalytic reactions on UiO-66 type of materials have been very successfully modeled using extended cluster models. We illustrate in Figure 40.5 an extended cluster for UiO-66 and UiO-66-NH_2 where only four linkers sharing the same plane are explicitly retained in the cluster to surround the active site. The remaining seven linkers were replaced by formic groups. Note that the extended cluster is constructed from a unit cell with one terephthalate defect, resulting in two active Zr-sites with a coordination that is reduced from 8 to 7. These Zr-sites operate as Lewis acid sites and are encircled with green circles. Analogously, UiO-66-NH_2 was constructed by replacing a hydrogen atom by an amino group on each phenyl ring. These amine groups act as Brønsted base sites and indicated with pink circles in Figure 40.5b. These cluster models have shown their usefulness [57] but in a sense they are also limited. The cases we studied so far showed that such extended models are in many cases sufficient to describe the different reaction steps mechanistically as all directly involved ingredients to initiate the reaction are present, but subtle factors generated by the linker environment are not incorporated in the cluster, framework flexibility, or presence of

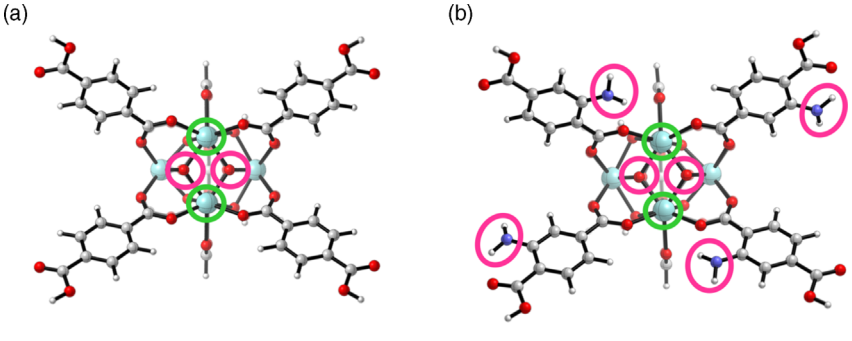

Figure 40.5 Cluster model with a Lewis acid site (encircled by green circles) and a Brønsted base site (encircled by pink circles) in UiO-66 (a) and UiO-66-NH_2 (b) with one linker defect. (Adapted with permission from Ref. [57]. Copyright 2015, Elsevier.)

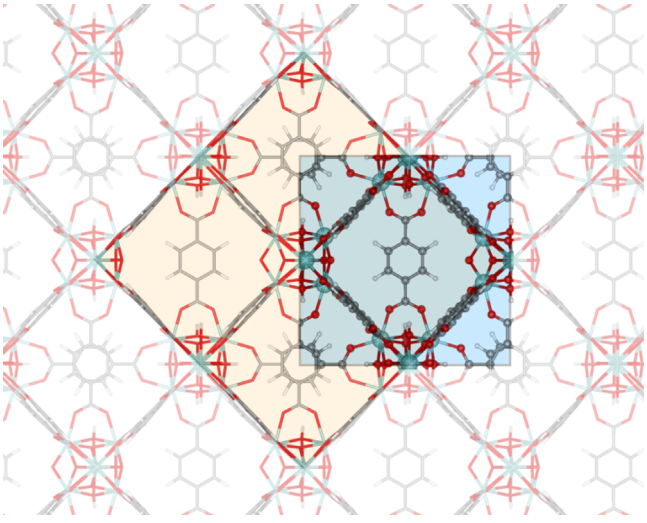

Figure 40.6 Conventional unit cell of UiO-66 with two linker defects: $<Zr_6O_6(OH)_2(RCOO)_{10}>_2$ $<Zr_6O_4OH_4(RCOO)_{12}>_2$. For computational feasibility a unit cell with only two Zr-bricks is frequently used, as indicated in blue.

assisting water molecules are not taken into account. If such factors are drastically affecting the mechanism or reaction rates, one can anticipate that such extended cluster models will not be able to reproduce these effects. We foresee that in the near future due to improvements of theoretical models and steady increase in computational power, more catalysis work within MOFs using periodic models and state of the art quantum mechanical models will be performed.

Indeed, as in zeolites the most appropriate model to describe a MOF is the periodic model. Unit cells of the periodic MOF structures may be of respectable size and at the limit of actual feasibility. To illustrate, Figure 40.6 shows the unit cell of a UiO-66 containing four inorganic Zr-bricks $<Zr_6O_4OH_4(RCOO)_{12}>$ and 24 BDC (terephthalate) linkers. $RCOO^-$ is a shorthand notation for half a BDC^{2-} linker. The coordination of each Zr-brick is 12-fold. UiO-66 can only be catalytically active if linker defects are present. In Figure 40.6, we visualize the unit cell of a two-linker defect generating four Zr-bricks with respective coordination number $CN_1 = 12$, $CN_2 = 10$, $CN_3 = 12$, and $CN_4 = 10$. The conventional unit cell with two linker defects comprises 456 atoms $- 2 \times 18$ atoms $= 420$ atoms among which 24 are Zr-atoms. This already gives an indication of the required computational cost. A geometry optimization with the periodic VASP code [63–66] for such an extended system with addition of frequency calculations demands a huge computation time but is presently in principle feasible. To reduce the computational time, a periodic unit cell consisting of only two Zr-bricks can be considered, which has been applied with success [57] but has of course its limitation as only a particular class of defect structures can be incorporated in this reduced periodic cell and periodic images are manifestly closer to

each other that generate unphysical perturbations. This is best visualized in Figure 40.6. In literature, most of the modeling activities on MOFs discuss their structural and thermal properties. Only a few papers deal with the modeling of a chemical reaction with the MOF as catalyst. Catalytic reactions in MOFs are not so abundant in literature and not so widely used as in zeolite catalysis. Another reason of this lack on theoretical work lies probably on the limitations of the cluster model and the too large unit cell for an adequate modeling of the active site. However, we demonstrate that the active site of a MOF can nowadays best be modeled by its periodic 3D structure. Linker deficiencies lead to Zr-bricks with different coordination numbers. Current modeling techniques are now able to handle them correctly in the right environment.

Summarizing, modeling a chemical reaction in the pores of a zeolite has been performed by several groups using the most advanced methods. The current toolbox delivers all required techniques to model the catalytic site in a correct way. We do not find the same activity in literature to model catalytic reactions in MOFs. We believe that there is no reason anymore to show any reluctance to handle MOFs in a first principles periodic model taking into consideration all features appropriate to MOFs, like the flexibility of the frame which is more pronounced than in zeolitic structures. However, it will probably take several years in order to apply such advanced models on these challenging systems in a mainstream way.

40.3
General Characteristics of a Heterogeneous-Catalyzed Reaction

Prior to reaction on a heterogeneous catalyst, at least one of the reactants has to adsorb at the active site. Thus, before being able to model a reaction – or to determine a reaction path along a well-defined reaction coordinate – dedicated simulations are needed to elucidate the characteristics of the adsorption complexes from which the reaction starts. These calculations also yield information on the surface coverage, which is important information when comparing theoretical data with experimental kinetic measurements. Indeed, the reaction rate depends on the fractional coverage of active sites by the reactants. A schematic illustration of the reaction profile for a typical zeolite-catalyzed reaction is shown in Figure 40.7. In particular, Figure 40.7 displays the reaction profile for propene methylation on an acidic zeolite which is an important reaction step in the methanol-to-olefin (MTO) process. Experimentally, one measures the apparent activation energy (denoted as $\Delta E^{\ddagger}_{\mathrm{app}}$ in Figure 40.7). From Figure 40.7, it becomes clear that it is crucial to obtain proper adsorption data of reactants from a computational perspective to enable the direct comparison of theoretical rate constants with experimental data. As such, the experimentally measured apparent activation energies and reaction rates should not be compared with the calculated intrinsic barriers and rates but with apparent kinetic data.

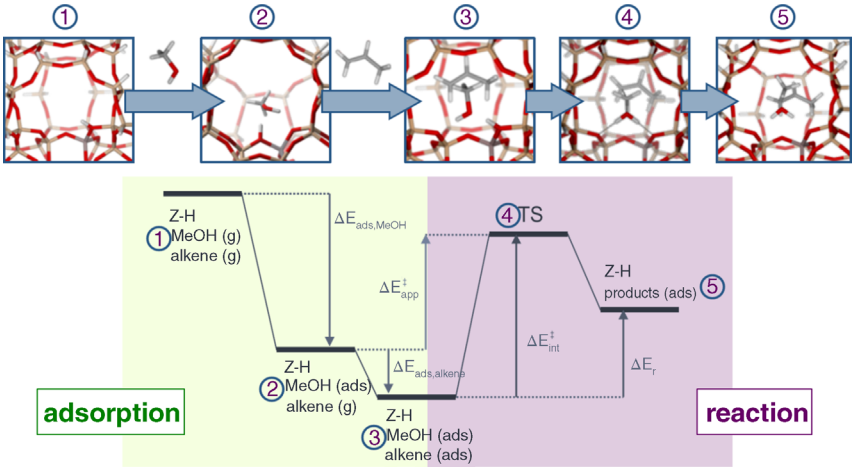

Figure 40.7 Schematic reaction profile of propene methylation over an acidic zeolite catalyst with indication of adsorption and reaction steps.

40.3.1 Determining Critical Points Along the Reaction Pathway: Adsorption

As described above, an accurate description of adsorption in nanoporous materials is mandatory during the process of modeling heterogeneously catalyzed reactions. Various critical points along the reaction profile need to be determined theoretically and this can be done using a variety of theoretical models. As discussed in the previous section, the modeler first needs to decide on the way in which the catalyst itself will be described, that is, cluster/periodic. Once this choice is made, a next decision concerns whether the reaction profile will be modeled using static methods or methods that allow sampling of larger portions of the potential energy surface (PES). Static methods refer to techniques that only consider a limited number of points on the potential energy surface. In case of the previous reaction profile regarding propene methylation over an acidic zeolite catalyst (Figure 40.7), five states need to be described. The advantage of static approaches consists in their simplicity as only a limited number of points are necessary and these can be described with a high accuracy. However, for some catalytic processes this approach clearly fails, as one can simply not identify one reactant state. Moreover, the structure/appearance/stability of intermediates is also sensitive to the operating conditions such as reaction temperature and pressure. In static methods the stability of intermediates at finite temperature is based on properties of the potential energy surface at 0 K. In order to clarify this item, we illustrate the advantage/disadvantage of static methods to describe the adsorbed state of the reactants.

A good example concerns the adsorption of alkenes in zeolites, which is a very challenging case both for theoreticians as for experimentalists due to the high

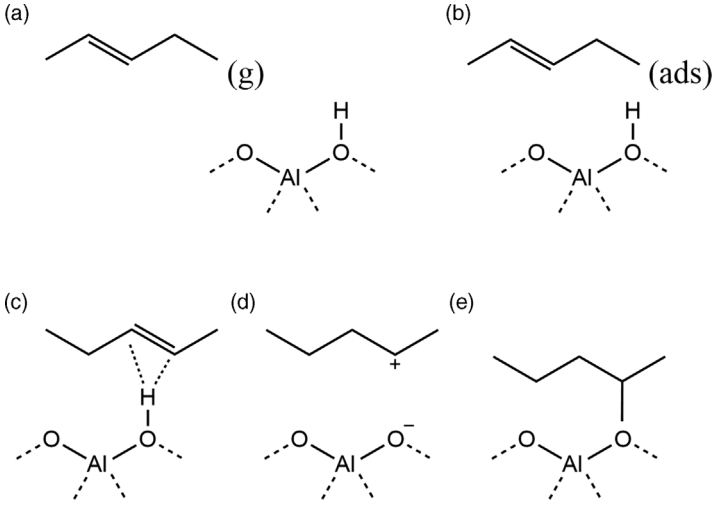

Figure 40.8 Illustration of the different intermediates upon alkene (2-pentene) adsorption in the presence of a Brønsted acid site (BAS): (a) alkene in gas phase, (b) alkene physisorbed in the channels of the zeolite (c) alkene π-complex, (d) chemisorbed carbenium ion (e) chemisorbed alkoxide.

reactivity of the intermediates even at low temperatures. When an alkene adsorbs on a Brønsted acid zeolite, various adsorbed species may be distinguished as schematically indicated in Figure 40.8 [67–70]. A first state corresponds to a free alkene in the cages of the zeolite, which undergoes only a weak van der Waals (vdW) interaction with the walls of the zeolite. This state is further referred to as the physisorbed state. A more bound state corresponds to the π-complex, where a specific nonbonded interaction between the π-electrons of the double bond and the Brønsted acid site occurs. Finally, the π-complex may be protonated leading to the formation of a chemisorbed species [67–70]. The nature of the resulting intermediate is still debated. It has been proposed to be stabilized as a covalently bonded alkoxide or as an ion pair that is referred to as a free carbenium ion (Figure 40.8) [67,68,71,72,83].

Solely based on experiment, it is practically excluded to gain insight into the nature of the adsorbed complexes and intermediates, which can be very short-lived. Thus, modeling may be an ideal complement to get track of these adsorbed species. However, in this case we are confronted with a rather mobile molecule in the pores of the zeolite and it is very difficult to pinpoint one specific minimum on the PES at 0 K. In reality, the PES is very flat yielding a multitude of almost isoenergetic minima. To deal with this complexity, one might sample the phase space with more advanced methods such as molecular dynamics (MD) methods. An extra asset of these methods is that they allow to take into account the flexibility of the material at realistic conditions of temperature and pressure. Depending on the statistical ensemble chosen during the simulation, that is, NVT or NPT ensembles, one samples the system either under fixed

conditions of cell volume and temperature or pressure and temperature. A more detailed explanation on statistical mechanics can be found in the reference work of Frenkel and Smit [73]. However, it needs to be mentioned that excessively long simulation times are necessary to obtain statistically relevant average ensembles. Taken into account that these exercises are best done using high-level quantum mechanical-based methods, it is easily understood that such approach can not be regarded yet as the method of choice for daily applications. In case of pentene adsorption in H-ZSM-5, we determined probability distributions of some critical distances in molecular dynamics simulations of π-complexes and alkoxides in H-ZSM-5 obtained over a 60 ps run. The resulting probability distribution is shown in Figure 40.9.

The distribution of the 1-pentene π-complex is interesting as the distribution is rather asymmetric toward longer interaction distances of the alkene bond and the Brønsted acid site. This means that at finite temperature the complex will on average be positioned slightly further away from the acid site than predicted from static calculations at 0 K. Furthermore, various orientations of the alkene with respect to the acid site and the zeolite walls are accessible. To determine adsorption enthalpies from these simulations various methods can be applied. One can opt to select some frequently sampled structures from the MD simulation and perform static energy refinements on these complexes or one could

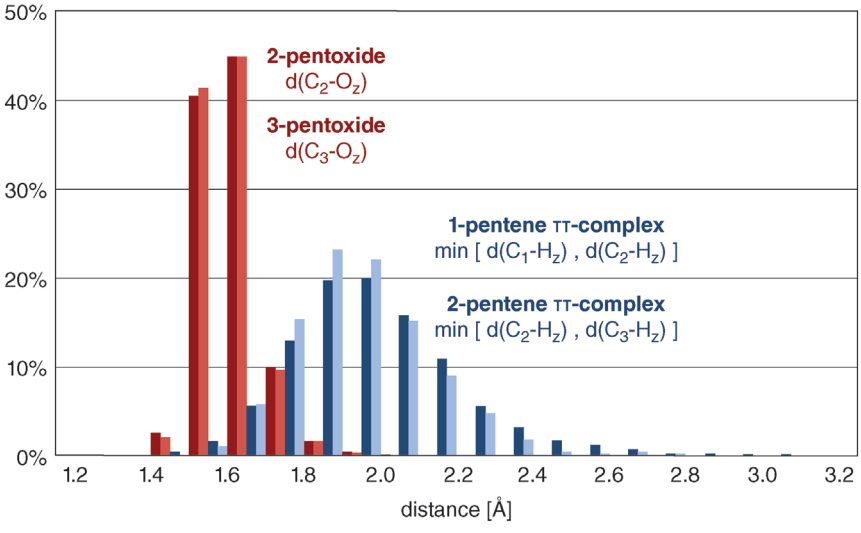

Figure 40.9 Probability distributions of some critical distances in molecular dynamics simulations of π-complexes and alkoxides in H-ZSM-5 obtained over a 60 ps run. Min[d(C_1-H_z), d(C_2-H_z)] stands for the shortest C-H_z distance in 1-pentene π-complex (average 2.07 Å); Min [d(C_2-H_z),d(C_3-H_z)] stands for the shortest distance in the 2-pentene π-complex (average: 2.04 Å); d(C_2-O_z) is the C_2-O_z distance in 2-pentoxide complex (average: 1.62 Å); and d (C_3-O_z) is the C_3-O_z distance in 3-pentoxide complex (average: 1.62 Å). (Reproduced with permission from Ref. [74]. Copyright 2016, Elsevier.)

deduce the adsorption enthalpies from the molecular dynamics simulations themselves. Strictly spoken this last procedure might be preferred, but our experience learns that excessively long simulation times are necessary to achieve converged values for the adsorption enthalpies. Furthermore, the overall computational cost of an MD simulation is determined by the level of theory chosen to determine the energies and forces. At present, *ab initio* MD simulations based on DFT are mostly performed with gradient-corrected exchange-correlation functionals complemented with dispersion forces not involved in the DFT functionals. More advanced functionals or other high-level electronic structure methods can certainly enhance the accuracy of the deduced adsorption enthalpies from MD simulations, but these calculations are very demanding and a reduction of the total simulation time to partly compensate for the huge computational time is not an optimal solution. More information on the level of theory is given in Section 40.3.2 of this chapter.

Previous discussion shows that the study of a complex chemical transformation ideally combines the advantages of static and dynamic approaches, as both methods have their merits and deliver complementary information.

The advantages of static approaches relate to the fact that most advanced levels of theory are available to describe the energies of the system. A good simulation of the adsorption of guest molecules inside the pores of a nanoporous material requires an accurate description of noncovalent interactions such as electrostatic, hydrogen bonding, and van der Waals interactions between the guest molecules and the host material. Density functional theory methods are the method of choice to treat large systems, as they offer a favorable balance between accuracy and computational efficiency. However, a general drawback of commonly applied local density functionals is that they cannot describe long-range electron–electron correlations that are responsible for the dispersion forces. The latter are in many works colloquially named van der Waals forces. In most of the functionals the missing dispersion forces are added as correction terms, while in some contemporary DFT functionals attempts have been made to incorporate dispersion directly by inserting specific terms and by an appropriate parameterization of the functional parameters. A short discussion of the frequently used DFT levels of theory in recent works is presented in Section 40.3.1.1.

40.3.1.1 Levels of Theory (LOTs) in Periodic Codes

Nowadays, many codes are available offering a plethora of theoretical techniques to study the energies of a periodic system. We can illustrate this point based on our experience with VASP calculations. The VASP package [63–66] is one of the major software codes available to perform calculations on periodic structures of framework materials using a whole scope of different levels of theory [23,36,75,76]. As already mentioned, gradient-corrected exchange-correlation functionals are largely preferred in geometry optimizations such like PBE [77], BLYP, and revPBE [78] with D3 corrections of Grimme [35] for the missing dispersion forces. While hybrid DFT functionals with exact exchange like B3LYP are currently implemented in VASP, they are not systematically used

in the geometry optimization of the extended system but only at the final stage for energy refinements. The only plausible reason is the high computational cost for a hybrid functional, which does not necessarily lead to better geometries of the complex consisting of a periodic nanoporous material and some guest molecules in the pores. There exists a general consensus that the plane wave kinetic energy cutoff may be not lower than 600 eV (for zeolites) and 500 eV (for MOFs) when applying the projector augmented approximation (PAW). The criterion for energy convergence may not be larger than 10^{-7} eV. Further, in literature there exists a lot of inconsistency whether or not the unit cell should be relaxed during the geometry optimization. Relaxation energies can easily rise up to 25 kJ mol^{-1} per unit cell, suggesting a consistent use of the optimization procedure in the entire cycle of calculations to avoid numerical inaccuracies that can rise to unphysical proportions when subtracting binding energies from each other as is the case for the computation of adsorption enthalpies.

While D3 is generally accepted to be a reliable correction scheme for dispersion, especially in combination with PBE and revPBE, other contemporary dispersion models are available and easily handled in the energy refinement procedures like BEEF-vdW [79], PBE with the new many body dispersion (MBD) scheme of Tkatchenko with conventional (MBD-vdW-H) and iterative Hirschfeld partitioning (MBD-vdW-HI) [80,81].

DFT is no longer the only feasible many-particle methodology in periodic codes, very recently other many-body perturbation methods like the random-phase approximation (RPA) are implemented in the VASP code. RPA contains dynamic electron correlations combining long-range dispersive and short-range exchange effects by continuously changing from the Kohn–Sham Hamiltonian to the exact many-body electron–electron interaction [82]. The exchange-correlation energy can thus be extracted from the electronic response in an (in principle) exact way. Actually, the number of effective applications of RPA on periodic nanoporous materials is rather limited. We refer to a successful application on alkane adsorption in Na-exchanged chabazites [83]. In this work, RPA outperforms by far DFT-based methods even with the most advanced exchange-correlation functionals. Highly accurate electronic-structure methods like RPA have not been applied so far on MOFs, although calculations are under way to improve the understanding of energetic and mechanical behavior of framework materials.

This brief overview shows that from a methodological point of view a plethora of methods are available to study reactions in periodic static models. The only obstacle for usage of computationally very expensive methods on a regular basis is the computer time and the large number of atoms one is often confronted with for realistic models (easily adding up to 500 atoms per unit cell in MOFs). Extended cluster models were quite often used in the past but lose their attractiveness in this matter as higher levels of theory do not compensate the lack of a correct description of the nanoporous environment.

While static periodic calculations can be performed at the highest level of theory, this is by far not the case in molecular dynamics simulations. This

emphasizes the complementarity between the two approaches. The focus of MD is different, and the information gathered after a MD run can be captured as input for a static calculation at a higher LOT.

To illustrate the complementary features obtained from static and molecular dynamics simulations, a summarizing adsorption enthalpy diagram for various adsorbed complexes of pentene is given in Figure 40.10. Adsorption enthalpies obtained from static calculations at 0 K are systematically larger than

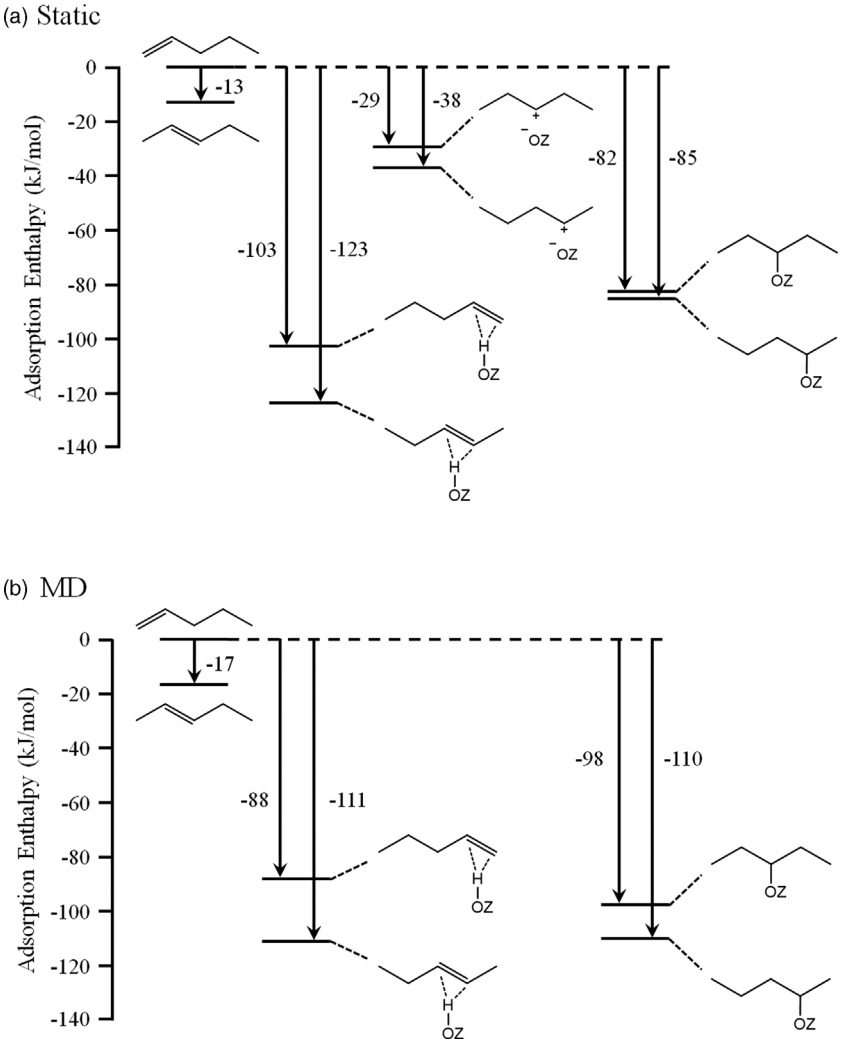

Figure 40.10 Adsorption enthalpy diagrams at 323 K for the several pentene intermediates with reference to 1-pentene in gas phase and an empty H-ZSM-5 framework obtained from (a) static calculations at the PBE-D3 level (b) MD simulations at the revPBE-D3 level. (Reproduced with permission from Ref. [74]. Copyright 2016, Elsevier.)

dynamically averaged values, since only the optimized structure of the π-complex at 0 K is taken into account. Thermal fluctuations on the relative distance of the complex with the Brønsted acid site give a better representation of the dynamical adsorption process and give adsorption enthalpies which are on average 20–30 kJ mol^{-1} less stable compared to their static values. Static periodic calculations have the advantage that they allow to use a large variation of DFT functionals and dispersion models. Göltl *et al.* observed same features for the adsorption behavior of alkanes and proposed to dynamically weight statically obtained adsorption enthalpies [83]. Based on our observations this might indeed be a good practice for future adsorption studies.

40.3.2 Identifying Transition-State Regions for Complex Chemical Transformations

To finally study the chemical conversion itself, one needs to identify transition-state regions. To this end, a reaction coordinate needs to be identified that leads the system smoothly from the reactant to the product region. It corresponds to that specific generalized coordinate for which maximum energy is reached during the transition from reactants to products. In its simplest form, the reaction coordinate corresponds to a single bond length or bond angle. For more complex reactions, however, the reaction coordinate is multidimensional and can only be approximated by a combination of bond lengths and/or bond angles, or even by nongeometric parameters such as bond orders or coordination numbers.

When studying chemical reactions with static methods, one needs to identify the transition state or activated complex, which is a minimum in all directions except for one coordinate that leads the system from the reactant to the product valley. To identify transition states, no single well-determined recipe is available and it needs a very experienced user to localize these critical points along the reaction path. Transition state optimization routines are still much better equipped in molecular-based programs such a Gaussian [84] than in periodic solid-state codes. Therefore, one often opts to first localize critical points along the reaction path using extended cluster models and then import these geometries in periodic codes. An example of a transition state that was first localized in cluster-based models and then transferred to periodic frameworks is shown in Figure 40.11. Herein, the unit cell of UiO-66 is displayed with one missing linker and a reactive complex with two adsorbed species: benzaldehyde and propanal. The figure gives an indication of the complexity of the active site (encircled) and of the necessity to use the conventional unit cell of 4 Zr-bricks (orange cell in Figure 40.6), or the reduced cell with only two Zr-bricks (blue cell in Figure 40.6) as applied in Figure 40.11.

The transition state TS1 is part of a reaction pathway corresponding to the aldol condensation between benzaldehyde and propanal, which is taken as a model reaction for the condensation reaction to form the jasminaldehyde condensation product from benzaldehyde and heptanal [57]. Experimentally it was shown that under certain conditions, Zr-terephthalate MOFs (UiO-66) are

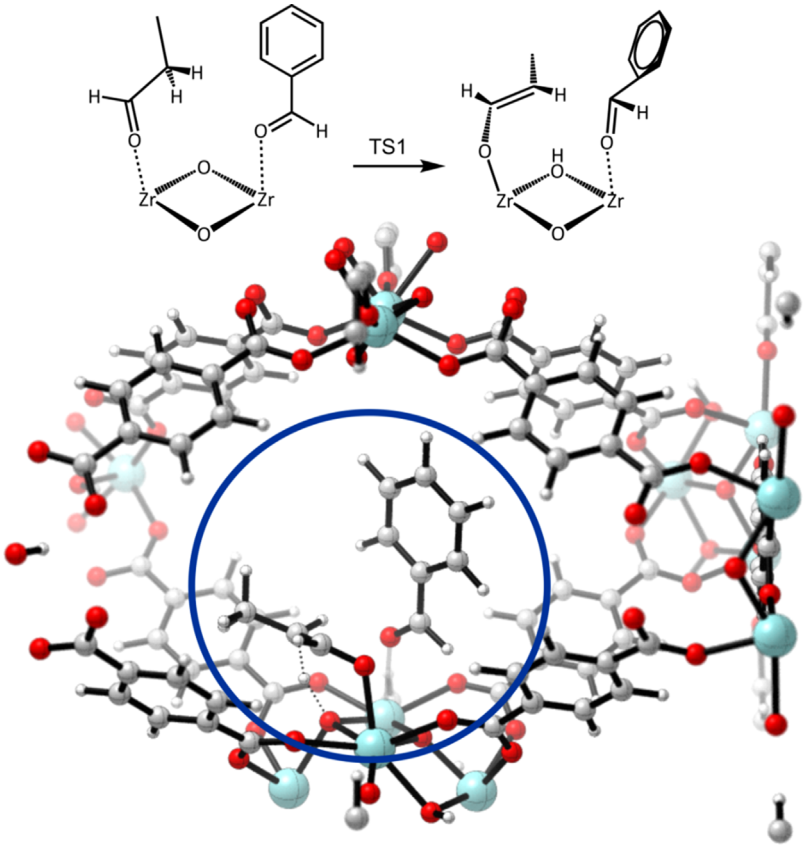

Figure 40.11 Adsorption of benzaldehyde and propanal at the Lewis acid site (Zr-atom) as a reactive complex before the aldol condensation. As material, we consider here UiO-66 with some linker defects to create an active site on a Zr-brick. (Reproduced with permission from Ref. [57]. Copyright 2015, Elsevier.)

highly selective catalysts for this cross-aldol condensation. However, it was very difficult to propose the exact reaction mechanism. Therefore, we performed density functional theory calculations on an extended cluster to elaborate on a plausible reaction pathway that is schematically shown in Figure 40.11. Once the whole aldol condensation reaction mechanism has been unraveled in the cluster approach, further refinement can be accomplished with periodic models accounting properly for the topology of the UiO-66 material. By illustration the free energy profile obtained with periodic models is also displayed in Figure 40.12 allowing a comparative study with the cluster results. Qualitatively, the main features of the reaction scheme are preserved, although quantitatively relatively large differences are found for the adsorption steps. For a more mechanistic discussion of the reaction – which is not the objective of this chapter – the interested reader is referred to the original paper [57].

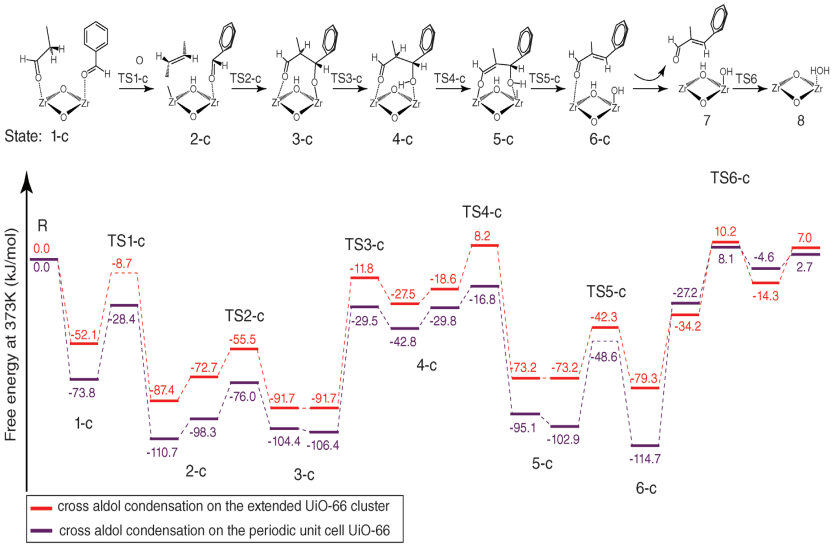

Figure 40.12 Schematic representation of the cross aldol condensation. Comparison of the free energy profiles between two models, cluster (red) and periodic (violet) UiO-66 for the jasminaldehyde condensation, calculated at 373 K. Level of theory on the cluster: B3LYP/6-311++G(d,p)-D3//B3LYP/6-31G(d)*. Level of theory on the periodic unit cell: B3LYP-D3(BJ)//PBE-D3(BJ). R corresponds to the reactants in gas phase and the cluster, P corresponds to the final product and water in gas phase and the cluster. (Reproduced with permission from Ref. [57]. Copyright 2015, Elsevier.)

This is a typical example of a reaction where the initial exploration of various transition states needs to be done in a computationally efficient way (use of extended cluster models) since a lot of intermediates and transition states are involved.

Summarizing, the periodic model, in which we account for the environment of surrounding linkers and other Zr Lewis acid sites, gives a more accurate description of the system. However, the qualitative aspects of the mechanism are fairly well described by the extended cluster model.

A side note, which is very relevant here, concerns the validation of the correct transition states. This should be done using a normal mode analysis. A correct transition state should be characterized by all positive frequencies except for one mode that leads us along the reaction coordinate. Performing a normal mode analysis within periodic codes is very challenging, one often is confronted with small negative frequencies which are due to global modes of the system and the nature of the PES which may be very flat. It may be very time consuming to remove all of these low-lying spurious frequencies, but in principle this elaborate work needs to be done to localize and identify the true transition state. Moreover, when it is the aim to calculate free energies and kinetic data it is of utmost importance that normal modes with low frequencies are properly described as they have a significant contribution to the vibrational partition function (*vide infra*). In literature we observe that some authors substitute these low-lying frequencies artificially with some value varying between 12 and 30 cm^{-1} to perform the thermochemical analysis.

The previous example was a showcase example of a complex reaction due to many reaction steps and the complexity of the molecular environment. However, in this case it was possible to identify proper transition states using static methods. In some cases it might be more difficult to use this methodology and one needs to use more advanced techniques that sample rather transition state regions instead of one single transition state. Hereafter, we show some applications of these more advanced techniques in zeolite catalysis to illustrate the workflow one needs to follow in such case.

We consider the methylation reactions of aromatic species in zeolites with various topologies. The general reaction scheme is given in Figure 40.13.

The methylation reaction of benzene with methanol can occur via two pathways, a direct path in which the methyl group of the methanol is transferred in one step to the aromatic species or an indirect route in which first a methoxide species is formed playing the role of a methylating agent in the second step. It has been shown in literature that the two pathways might become competitive at certain operating conditions [10,85,86].

In a first example, we show some modeling results of this methylation reaction in H-ZSM-5 but at various loadings of methanol molecules. Indeed, the standard way of studying this reaction accounts for only one methanol molecule; however, at realistic operating conditions, more methanol molecules may be present in the pores of the zeolite and these may change the overall reactivity. This example is a typical case where static methods fail in describing the situation whereby more

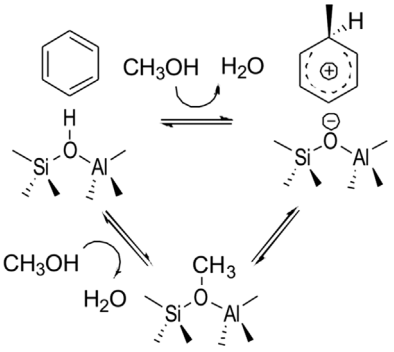

Figure 40.13 Schematic representation of the reaction mechanism of the zeolite-catalyzed methylation of aromatic species. (Adapted with permission from Ref. [11]. Copyright 2015, Wiley-VCH Verlag GmbH.)

than one methanol molecule is in play. It is realistic to imagine that multiple geometries are present in the description of reactant complexes and transition states with nearly equal energy and that the concept of one-single geometry fails as is standard in static approaches. It is a showcase example where molecular dynamics studies can offer an enormous added value compared to static methods.

Figure 40.14 shows the free energy profile for the concerted methylation of benzene in H-ZSM-5 with 5 methanol molecules with selected conformations representing four phases along the reaction pathway. It seems that prior to reaction methanol clusters can be present (phase I in Figure 40.14). The methanol that transfers its methyl group to the aromatic molecule then first has to escape the cluster conformation (phase II) to be able to undergo the actual methylation reaction (phases III and IV). The identification of these four phases originates from the dynamical approach applied in this study [13].

It should be noted that, in order to study reactions with a dynamical approach, regular MD simulations are often not able to sample transition state regions. Indeed, chemical transformations are rare events as their probability of occurence is very low, although once it occurs the event may be followed during a regular MD run of a few picoseconds. To enhance sampling of interesting regions of the free energy surface a multitude of methods has been developed [23]. The example shown above has been performed using the metadynamics (MTD) approach developed by Laio and Gervasio [87] and Laio and Parrinello [88]. The concept of such metadynamics approach is illustrated in Figure 40.15. It relies on the choice of a limited number of collective variables along which the free energy landscape is filled up with Gaussian hills to accelerate sampling of events. Afterwards the sum of the Gaussians defines a bias potential for the simulations that can be used to reconstruct the free energy surface. To date, the method is well developed and implemented in a series of computer packages such as CP2K, CHARMM, and so on. The usage however of the

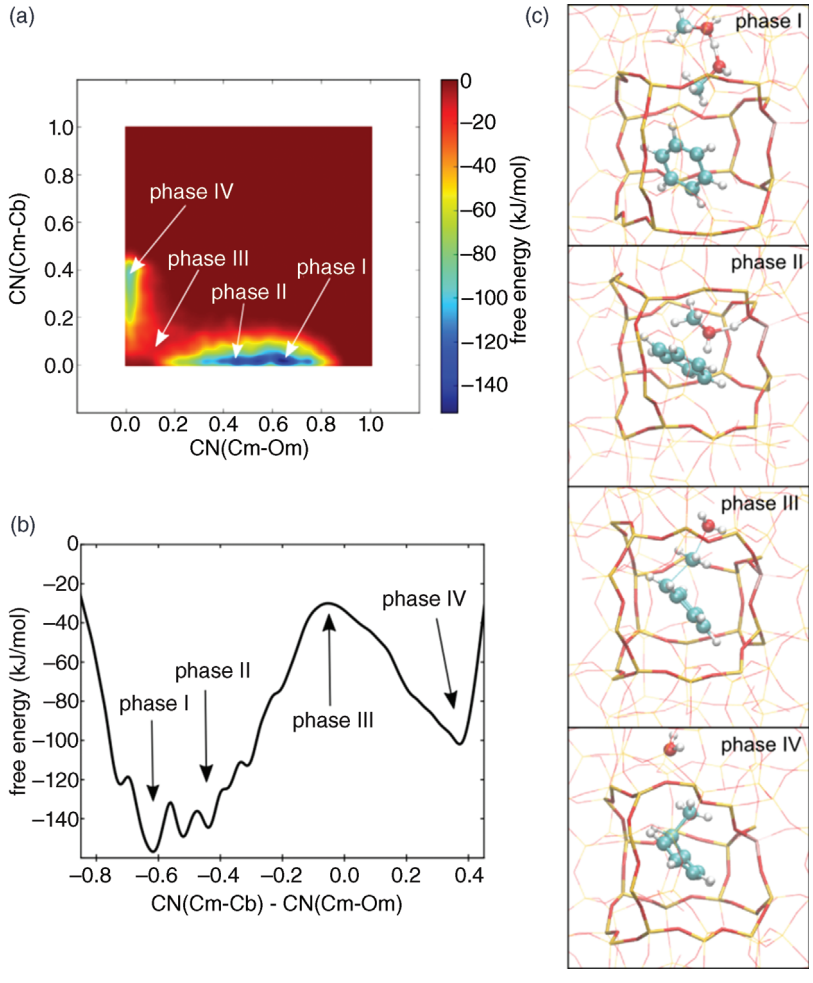

Figure 40.14 2D (a) and 1D (b) free energy profile for the methylation of benzene in H-ZSM-5 with five methanol molecules with selected conformations representing the four phases along the reaction pathway (c). Methanol molecules that do not participate in the reaction are not shown. (Reproduced with permission from Ref. [13]. Copyright 2013, the American Chemical Society.)

method for applications in nanoporous materials is rather limited. The practical execution requires special skills from the user, which are not available in a toolbox. For reactions occurring in the pores of a zeolite, the MTD methodology has been applied for the first time by Moors *et al.* [13] and more recently by De Wispelaere *et al.* [10,12,76]

As described above, a dynamical approach is beneficial in cases where multiple guest molecules make the reaction environment more complex. Another

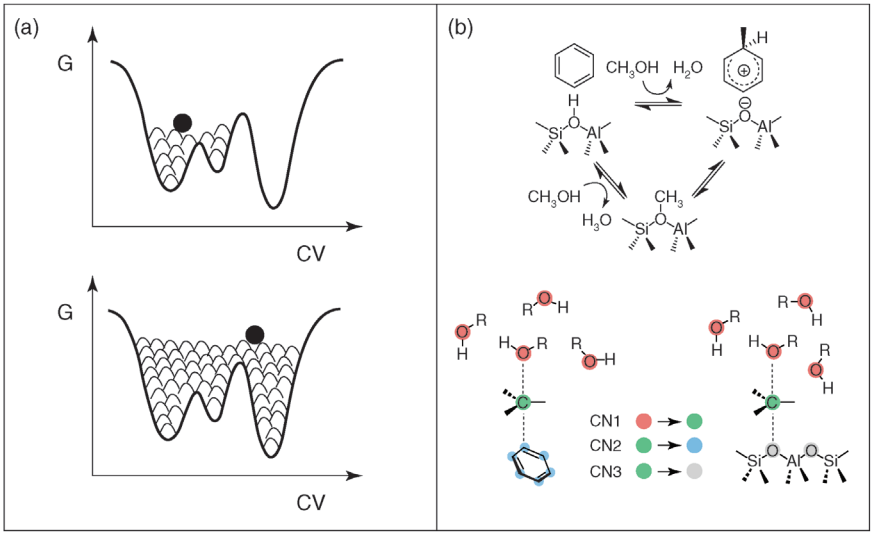

Figure 40.15 Gaussian hills construct the bias potential during a metadynamics run (a). To describe competing reaction paths, a high number of atoms should be included in the collective variables as illustrated for a methylation pathway (b). (Adapted from Refs. [10,11,23] with permission from the Royal Society of Chemistry and Wiley-VCH Verlag GmbH.)

important example is when broad reactant state and transition state regions can be expected. To illustrate this, we again consider the methylation of benzene by methanol, but this time in the large pore zeolite H-SSZ-24. Due to its unidirectional 12-ring channel, this material gives a lot of configurational freedom to the guest molecules at high temperature (623 K in this case) [11]. With the metadynamics approach, a plethora of geometrically inequivalent and nearly isoenergetic transition states have been sampled as can be seen in Figure 40.16. It is obvious that all these configurations have an impact on the calculated free energy barriers and kinetic data for this reaction. Moreover, in this work the concerted and stepwise methylation reaction (cfr. Figure 40.13) have been sampled in one single run in order to explicitly account for the potential competition of both reaction mechanisms at elevated temperature. It was indeed confirmed that both reaction pathways exhibit nearly identical free energy barriers under these conditions.

The success of MTD critically relies on a proper choice of the collective variables, which enable us to walk on a privileged minimum energy path on the free energy surface, but MTD has also its limitations. MTD requires some prior knowledge of the reaction mechanism, but as a result of this knowledge one introduces some bias in the multiple constraints imposed during an MTD run. Another issue concerns the accuracy one may obtain using metadynamics methods. To our opinion, some dedicated benchmark studies are necessary to validate the method for well-studied reactions in zeolite catalysis. Such studies are underway.

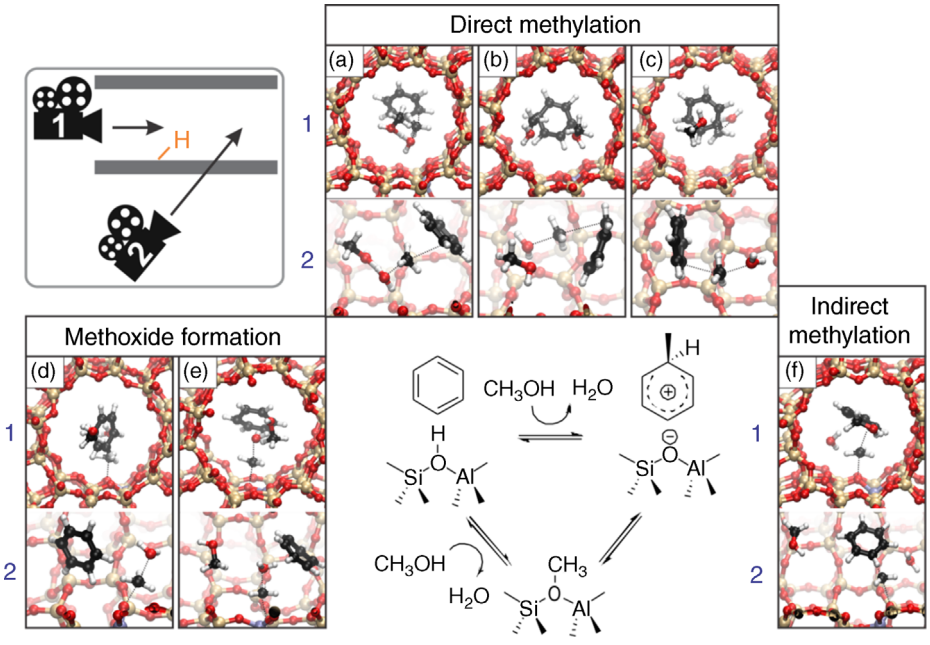

Figure 40.16 Snapshots of the concerted (a–c) and stepwise methylation (d–f) of benzene by two methanol molecules in H-SSZ-24 at 623 K, seen in the direction of the 1D channel (camera viewpoint 1) and in a cross section of the channel (camera viewpoint 2). (Adapted from Ref. [10] with permission from the Royal Society of Chemistry.)

Among other advanced MD techniques without prior knowledge or specification of transition states belongs transition path sampling which combines Monte Carlo moves on MD trajectories [89,90]. Hereby, reaction paths or trajectories are generated between reactant and product valley (see Figure 40.17). By means

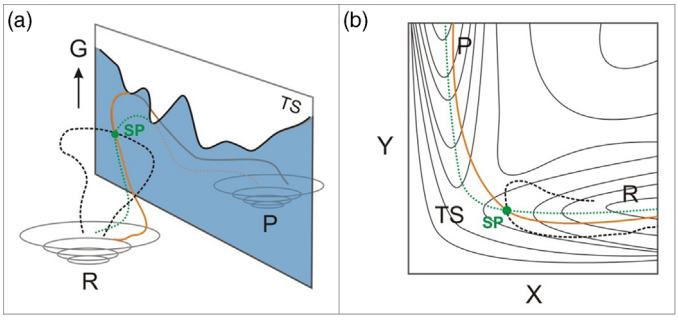

Figure 40.17 Schematic representation of the free energy landscape with two stable wells separated by a transition state ridge (a). From the initial path (full orange line) a new reactive trajectory (green dotted line) is shot from shooting point SP. The black dashed line represents a nonreactive trajectory (a). Part (b) shows the same trajectories on contours of a potential energy surface. (Adapted with permission from Ref. [92]. Copyright 2013, the Royal Society of Chemistry.)

of perturbations on an initial trajectory between R and P one creates new paths and thus finally one disposes of an ensemble of transition paths. From the dynamics of each path in the ensemble an ensemble averaged reaction rate coefficient can be determined [90]. This method has shown to be very successful especially in the modeling of zeolite-catalyzed reactions as demonstrated by Bučko *et al.* [91]

40.4
First Principle Chemical Kinetics from Static and Dynamic Calculations

The determination of rate constants of elementary chemical reactions taking place in nanoporous materials from first principles has reached such a level of accuracy that molecular control over production processes (yield, selectivity, etc.) by theory is achievable. A lot of theoretical papers within zeolite and MOF catalysis primarily focus on various mechanistic aspects of the catalytic reactions. Herein, reaction barriers play an essential role.

Key property of chemical kinetics and the determination of the rate constant is the Gibbs free energy barrier that differs in its computation in static and dynamic calculations. In the latter a large number of states is sampled, and an averaging over all samples yields quantities that satisfy statistical grounds provided phase space is sufficiently sampled during the dynamic simulation. This methodology is the only correct procedure if sufficiently large simulation times are respected. Currently, the explosive expansion of computer capabilities enables the performance of such large simulations on extended and complex systems, but it is clear that this procedure is not appropriate as standard method of choice for any catalytic reaction taking place in the pores of a nanoporous material. In most cases one falls back to the reproduction of the three stationary points, which initial structures are inspired by the various reaction paths suggested in the MD simulations.

40.4.1
Static Approach –Transition State Theory (TST)

Within the static approach, the reaction is described by three stationary points: the reactive complex, the TS complex, and the product complex. All stationary points are determined at 0 K. For most catalytic reactions in the pores of a nanoporous material, the PES is very flat and multiple reactive complexes – differing with some few $kJ\,mol^{-1}$ – are valuable candidates as reactant in the static approach of the reaction. As outlined in previous sections, standard AIMD simulations can assist in extracting suitable initial structures for the geometry optimization of the adsorbed complexes. Important issue is that a static optimization reflects the situation at 0 K, with the consequence that the found equilibrium distances characterizing the reactant complex do not correspond with the real situation which takes place at finite

temperatures. This shortcoming can lead to over or underestimation of reaction barriers, and thus a serious shortcoming of the static approach. The further procedure in a static approach consists in evaluating the partition functions from the frequencies belonging to the geometries of the three stationary points. Note that the transition state or activated complex represents a saddle point on the multidimensional potential energy surface, that is, minimum in all degrees of freedom except in the reaction coordinate for which a maximum is reached.

The reaction rate constant is given by

$$k(T) = \frac{k_B T}{h} V^{-\Delta^{\ddagger} n} \, \mathrm{e}^{-\frac{\Delta^{\ddagger} G}{\mathrm{RT}}} = \frac{k_B T}{h} V^{-\Delta^{\ddagger} n} \, \mathrm{e}^{\frac{\Delta^{\ddagger} S}{R}} \mathrm{e}^{-\frac{\Delta^{\ddagger} H}{\mathrm{RT}}}. \tag{40.1}$$

In this expression, k_B represents the Boltzmann constant, T stands for the temperature, h is Planck's constant, and R is the universal gas constant.

For a unimolecular reaction $\Delta^{\ddagger} n = 0$ and the rate constant $k(T) = (k_\mathrm{B} T/h)\, \mathrm{e}^{-\frac{\Delta^{\ddagger} G}{\mathrm{RT}}}$ is expressed in s^{-1}.

For a bimolecular reaction $\mathrm{A} + \mathrm{B} \rightarrow (\mathrm{AB})^{\ddagger}$ ($\Delta^{\ddagger} X = X_{\mathrm{AB}^{\ddagger}} - X_\mathrm{A} - X_\mathrm{B}$) is $\Delta^{\ddagger} n = -1$ and the rate constant $k(T) = (k_B T/h)\, V\, \mathrm{e}^{-\frac{\Delta^{\ddagger} G}{\mathrm{RT}}}$ is expressed in units $\mathrm{dm}^3\ \mathrm{mol}^{-1}\ \mathrm{s}^{-1}$.

It is common to decompose the free energy of activation into the standard enthalpy of activation and the standard entropy of activation, following

$$\Delta^{\ddagger} G = \Delta^{\ddagger} H - T \Delta^{\ddagger} S, \tag{40.2}$$

with

$$\begin{aligned} \Delta^{\ddagger} H &= \Delta^{\ddagger} U_0 + \Delta^{\ddagger} U_{\mathrm{therm}} + \mathrm{RT} \Delta^{\ddagger} n \\ &= \Delta^{\ddagger} U + \mathrm{RT} \Delta^{\ddagger} n \end{aligned},$$

and thus

$$\Delta^{\ddagger} H = \Delta^{\ddagger} U - \mathrm{RT}, \tag{40.3}$$

for a bimolecular reaction as for a reaction of a gas with active site on a solid surface, and

$$\Delta^{\ddagger} S = R \ln\left(\frac{Q^{\ddagger}}{Q_\mathrm{A} Q_\mathrm{B}}\right) + \frac{1}{T} \Delta^{\ddagger} U_{\mathrm{therm}}. \tag{40.4}$$

In case of a bimolecular reaction in which one of the reactants represents a fixed framework (e.g., chemisorbed complex), that reactant does not contain translational nor rotational degrees of freedom.

We refer to the Appendices A and B for some thermodynamic expressions elucidating the above discussion.

The static frequency calculations for the two stationary states (prereactive complex and TS for the forward reaction) lead to the direct computation of the following:

- The electronic barrier ΔE_0 including zero point energies (ZPE) from the various vibrational modes

$$\Delta^{\ddagger}U_0 = \Delta E_0 = E_0^{\ddagger} - E_0^{\mathrm{A}} - E_0^{\mathrm{B}} + \Delta E_{0,\mathrm{vib}}$$

with

$$\Delta E_{0,\mathrm{vib}} = \sum_{i=1}^{N^{\ddagger}} \frac{1}{2} h\nu_i^{\ddagger} - \sum_{i=1}^{N_{\mathrm{A}}} \frac{1}{2} h\nu_i^{\mathrm{A}} - \sum_{i=1}^{N_{\mathrm{B}}} \frac{1}{2} h\nu_i^{\mathrm{B}}$$

- The partition functions $\left(Q^{\ddagger}/Q_{\mathrm{A}}Q_{\mathbf{B}}\right)$ defining the entropy of activation.
- The small thermal corrections $\Delta^{\ddagger}U_{\mathrm{therm}}$ that are also determined from the frequencies (see Appendices A and B).

Partition functions are unit less quantities, and thus also $\left(Q^{\ddagger}/Q_{\mathrm{A}}Q_{\mathrm{B}}\right)$ but its evaluation requires the value of the volume V by means of the translational partition functions. A further elucidation is obtained by factorizing the expression of the partition functions into translational and other degrees of freedom

$$\begin{aligned}\left(\frac{Q^{\ddagger}}{Q_{\mathrm{A}}Q_{\mathrm{B}}}\right) &= \left(\frac{Q^{\ddagger}}{Q_{\mathrm{A}}Q_{\mathrm{B}}}\right)_{\mathrm{trans}} \left(\frac{Q^{\ddagger}}{Q_{\mathrm{A}}Q_{\mathrm{B}}}\right)_{\mathrm{other}} \\ &= \left(2\pi \frac{m_{\mathrm{A}}m_{\mathrm{B}}}{m_{\mathrm{A}}+m_{\mathrm{B}}} k_{\mathrm{B}}T\right)^{-3/2} \frac{h^3}{V} \left(\frac{Q^{\ddagger}}{Q_{\mathrm{A}}Q_{\mathrm{B}}}\right)_{\mathrm{other}}.\end{aligned}$$

The reaction rate constant can then be expressed in the following form:

$$k(T) = \frac{k_{\mathrm{B}}T}{h} \left(2\pi \frac{m_{\mathrm{A}}m_{\mathrm{B}}}{m_{\mathrm{A}}+m_{\mathrm{B}}} k_{\mathrm{B}}T\right)^{-3/2} h^3 \left(\frac{Q^{\ddagger}}{Q_{\mathrm{A}}Q_{\mathrm{B}}}\right)_{\mathrm{other}} \mathrm{e}^{-\frac{\Delta E_0}{\mathrm{RT}}},$$

which clearly illustrates the V-independence of $k(T)$ but involving the correct dimension of $\mathrm{s}^{-1}\ \mathrm{dm}^3$ or $\mathrm{s}^{-1}\ \mathrm{m}^3$. By multiplying with the number of Avogadro N_{A} the bimolecular rate constant $k(T)$ can be expressed in units $\mathrm{s}^{-1}\ \mathrm{dm}^3\ \mathrm{mol}^{-1}$ as usual.

40.4.2 Dynamic Approach

Standard *ab initio* MD simulations are frequently used to explore the whole-phase space and to attain an almost complete sampling of the conformational space. This is of particular use in the exploration of the plausible complexes of reactants adsorbed to the active site of the catalyst.

Most often sufficiently long NVT simulations are run and they deliver ensemble averages of the internal energies obtained by averaging the sum of potential and kinetic energy. This procedure allows us to determine the adsorption energy for the adsorbed complex of reactant molecules by performing separate NVT

runs on the complex, the empty nanoporous material (zeolite, MOF) and the adsorbate in gas phase

$$\Delta U_{\text{ads}} = < E_{\text{complex}} > - < E_{\text{nanoporous}} > - < E_{\text{reactants}} > . \tag{40.5}$$

The corresponding adsorption enthalpies are then given by

$$\Delta H_{\text{ads}} = \Delta U_{\text{ads}} - \text{RT}, \tag{40.6}$$

in which R is the universal gas constant (at 323 K: RT = 2.7 kJ mol^{-1}).

As mentioned earlier, regular MD simulations cannot efficiently sample catalytic reactions for potential energy surfaces where the basins are separated by relatively high potential ridges. In this case advanced MD techniques are here required to enhance the occurrence of the rare event. They all incorporate constraints to guide the complex systems during the simulation along the desired reaction path. By these constraints the MD runs does not explore the complete potential energy surface anymore but rather a region around the minimum-energy path.

Constrained MD simulations give access to free energy profiles of chemical processes. By means of Eq. (40.1) rate constants may eventually be extracted. However, this implies that the free energy of activation should result from the simulations.

The MTD approach relies on the selection of a set of collective variables that describe the reaction under study. This often leads to multidimensional free energy surfaces, which are complex to interpret and from which it is difficult to extract a free energy barrier. We illustrate the approach to extract a free energy barrier based on a free energy surface for an MTD simulation with two collective variables which yields a 2D free energy surface. First, the 2D free energy surface can be projected onto a 1D profile according to the following:

$$G(\text{CV2} - \text{CV1}) = -\frac{1}{k_{\text{B}}T} \ln\left\{ \int_{-\infty}^{+\infty} \text{d}_{\text{CV1}} \exp\left[-\frac{1}{k_{\text{B}}T} G(\text{CV2} - \text{CV1}, \text{CV1}) \right] \right\}. \tag{40.7}$$

Alternatively, one can calculate the lowest free energy path (LFEP) on the calculated FES as described by Ensing and *et al.* [11,93].

Based on the one-dimensional free energy profile it is now essential to calculate the free energy for each state, that is, for the reactants, transition state region, and product state.

In Appendix B a brief summary of elementary concepts of statistical physics is given, which assists the reader in understanding the correct postanalysis of a MTD run.

Suppose that at the end of a MTD simulation we are able to deduce a 1D free energy profile $G_{\text{q}}(s)$ as function of a collective variable s. Free energy and partition function of a microstate q are related with the expression

$$G_{\text{q}}(s) = -k_{\text{B}}T \ln Z_{\text{q}}(s). \tag{40.8}$$

One could define a macrostate A for which s lies in the range (s_1, s_2). This gives rise to the following expressions:

$$Z_{\mathrm{A}} = \int_{s_1}^{s_2} Z_{\mathrm{q}}(s)\mathrm{d}s \tag{40.9}$$

$$G_{\mathrm{A}} = -k_{\mathrm{B}}T \ln Z_{\mathrm{A}} = -k_{\mathrm{B}}T \ln \frac{Z_{\mathrm{A}}}{Z} - k_{\mathrm{B}}T \ln Z. \tag{40.10}$$

In this case, Z_{A} must be interpreted as the contribution to the partition function from the macrostate A. Similarly, G_{A} can be interpreted as the free energy associated with the macrostate A which can be computed up to a constant G, which is the total free energy.

A more rigorous approach consists of dividing the complete range for s into the following three regions:

- The reactant region $\mathrm{R} = [-\infty, s_0]$
- The transition state region $\mathrm{TS} = [s_0, s_1]$
- The product region $\mathrm{P} = [s_1, +\infty]$

This partition can easily be extended if the trajectory encounters more than 1 TS.

Now we can compute

$$\begin{aligned} Z_{\mathrm{R}} &= \int_{-\infty}^{s_0} Z_q(s)\Delta s \frac{\mathrm{d}s}{\Delta s} = \int_{-\infty}^{s_0} \mathrm{e}^{-\beta G_{\mathrm{q}}(s)} \Delta s \frac{\mathrm{d}s}{\Delta s}; \quad G_{\mathrm{R}} = -k_{\mathrm{B}}T \ln Z_R \\ &= -k_{\mathrm{B}}T \ln \int_{-\infty}^{s_0} \mathrm{e}^{-\beta G_{\mathrm{q}}(s)} \Delta s \frac{\mathrm{d}s}{\Delta s}. \end{aligned} \tag{40.11}$$

$$\begin{aligned} Z_{\mathrm{TS}} &= \int_{s_0}^{s_1} Z_{\mathrm{q}}(s)\Delta s \frac{\mathrm{d}s}{\Delta s} = \int_{s_0}^{s_1} \mathrm{e}^{-\beta G_{\mathrm{q}}(s)} \Delta s \frac{\mathrm{d}s}{\Delta s}; \quad G_{\mathrm{TS}} = -k_{\mathrm{B}}T \ln Z_{\mathrm{TS}} \\ &= -k_B T \ln \int_{s_0}^{s1} \mathrm{e}^{-\beta G_q(s)} \Delta s \frac{\mathrm{d}s}{\Delta s}. \end{aligned} \tag{40.12}$$

$$\begin{aligned} Z_{\mathrm{P}} &= \int_{s_1}^{+\infty} Z_{\mathrm{q}}(s)\Delta s \frac{\mathrm{d}s}{\Delta s} = \int_{s_1}^{+\infty} \mathrm{e}^{-\beta G_q(s)} \Delta s \frac{\mathrm{d}s}{\Delta s}; \quad G_{\mathrm{P}} = -k_B T \ln Z_{\mathrm{P}} \\ &= -k_B T \ln \int_{s_1}^{+\infty} \mathrm{e}^{-\beta G_q(s)} \Delta s \frac{\mathrm{d}s}{\Delta s}. \end{aligned} \tag{40.13}$$

To circumvent the dimensionality conflict here, we introduced Δs and defined $Z_q(s)\Delta s = \mathrm{e}^{-\beta G_q(s)}$, which is inspired by the equation $G_A = -k_B T \ln Z_{\mathrm{q}}(\overline{s})\Delta s$.

Having introduced free energies to each region, we are now able to define free energies of activation $\Delta G^{\ddagger}$ as

$$\Delta G^{\ddagger} = G_{\mathrm{TS}} - G_R = -k_{\mathrm{B}}T \ln \frac{\int_{s_0}^{s_1} \mathrm{e}^{-\beta G_q(s)} \mathrm{d}s}{\int_{-\infty}^{s_0} \mathrm{e}^{-\beta G_q(s)} \mathrm{d}s} \tag{40.14}$$

and reaction free energies ΔG_r

$$\Delta G_r = G_P - G_R = -k_B T \ln \frac{\int_{s_1}^{+\infty} e^{-\beta G_q(s)} ds}{\int_{-\infty}^{s_0} e^{-\beta G_q(s)} ds}. \quad (40.15)$$

Δs drops out of the equation, so it does not influence the results.

The width of the TS region (s_0, s_1) is determined by the thermal fluctuation, which is given by the standard deviation of the collective variable s. We have systematically taken a value of 0.04, which represents the average of the thermal fluctuations measured at the local minima of the reactant valley.

From this discussion, it becomes clear that more complex models – for example, by applying a dynamical approach – also significantly increase the difficulty of data analysis. However, for some specific cases a dynamical approach seems mandatory to better mimic true reaction conditions.

40.5 Complementary Insights from Spectroscopy

Apart from modeling the reaction itself, computational spectroscopy has evolved as an indispensable characterization tool to identify intermediates during a reaction. *In situ* experiments deliver data, which evolve in time and vary with temperature and other operating conditions [94]. Infrared (IR), NMR spectra, and other optical spectroscopic techniques are continuously recorded and give crucial information on the reaction intermediates that have been formed in function of time, under condition that these experimental spectra are correctly interpreted. This indispensable toolbox is nowadays available due to the latest advances in the computation of the spectroscopic signals. It is not surprising that the most successful reproduction of spectroscopic spectra under real operating conditions come from molecular dynamics simulations.

Infrared spectroscopy is one of the leading characterization tools in zeolite and MOF chemistry covering the whole frequency range from low collective modes around 10 cm^{-1} to high frequency modes of bond stretches of about 4000 cm^{-1}. Vibrational frequencies of the eigenmodes of the system can be computed by construction of the Hessian matrix with the evaluation of the second-order derivatives of the total energy with respect to Cartesian displacements of the atoms in the system. In a static periodic calculation such a frequency calculation with 400 or more atoms is not a trivial task and needs some practical skills to construct an optimized unit cell of the catalyst (with and without adsorbed reactant molecules) with all positive frequencies. Not all current computational works apply the correct procedure in eliminating in an adequate way the appearing imaginary frequencies. They prefer a pragmatic approach by replacing each imaginary frequency by a low positive frequency (this value can vary from 12 to 30 cm^{-1}) [95,96]. It should be stressed that this procedure generates large errors

as low frequencies largely affect the vibrational partition functions leading to unphysical predictions for adsorption entropies and free energies. A static approach has further the disadvantage that all vibrations of the complex catalyst are treated within the harmonic approximation. Experimental vibrational and IR spectra are largely affected by anharmonicities and while they can also be incorporated in static approaches via nontrivial interventions [97], they are best taken into account in molecular dynamics simulations where anharmonicities of the modes appear in a natural way. But MD on such complex systems are confronted with a serious obstacle that long simulations are practically not feasible, at least when *ab initio* MD (AIMD) simulations are concerned. A valid alternative could be the use of classical force fields, which are developed for the material under investigation.

From the data recorded during the MD simulations infrared spectra can be obtained via the Fourier transformation of the dipole moment autocorrelation function $\langle d\overline{\mu}(0), \mu(t)\rangle$ leading to an expression for the IR adsorption cross section [98] $\alpha(\omega) \sim \lim_{\tau\to\infty} \frac{1}{\tau}\left|\int_0^\tau \mathrm{d}t\, \mathrm{e}^{-i\omega t}\frac{\mathrm{d}\overline{\mu}(t)}{\mathrm{d}t}\right|^2$.

As the time derivative of the dipole moment can be approximated as $(\mathrm{d}\overline{\mu}(t)/\mathrm{d}t) = \sum_{i=1}^{N} q_i\, \overline{v}_i(t)$ with q_i the charge and v_i the velocity of atom i, a simple velocity power spectrum (VPS) offers an adequate theoretical tool to construct a potential IR spectrum. In a comparative study with experiment focus lies into the position of the peaks rather than the intensities of the peaks.

We report here the results of two recent calculations of IR spectra based on VPS as explained above. First, we display an IR spectrum of NO adsorbed to copper-exchanged SSZ-13, which is known as an effective zeolitic material in the selective catalytic reduction of NO_x using ammonia [99]. Göltl *et al.* [99] used the theoretical model to unravel the complex multipeak infrared spectrum of NO. They performed different *ab initio* MD (AIMD) simulations using VASP at a finite temperature and for four sites differing in the position of the Al-atoms and the extra-framework cation Cu^{2+}. Each site leads to a specific multipeak IR-spectrum. In the experimental spectrum [100] shown in Figure 40.18 belonging to Cu-SSZ-13 with a Si/Al ratio of 6 and Cu/Al of 0.03, three broad bands are clearly observed. Various measurements have been done at different doses of NO, which is introduced stepwise into the cell per time interval. Dependent on the dose different peaks arise or disappear. By a suitable linear combination of the theoretically obtained VPS spectra an excellent agreement with experiment is observed, as shown in Figure 40.18b. For further information, we refer to Ref. [99].

For a complex system with reactant molecules adsorbed at the active site of a zeolitic frame or MOF framework, AIMD simulations within a periodic unit cell are only feasible for a relatively short simulation time (~50 ps). With the development of contemporary force fields, simulations times of some nanoseconds are not exceptional and these long runs have a beneficial

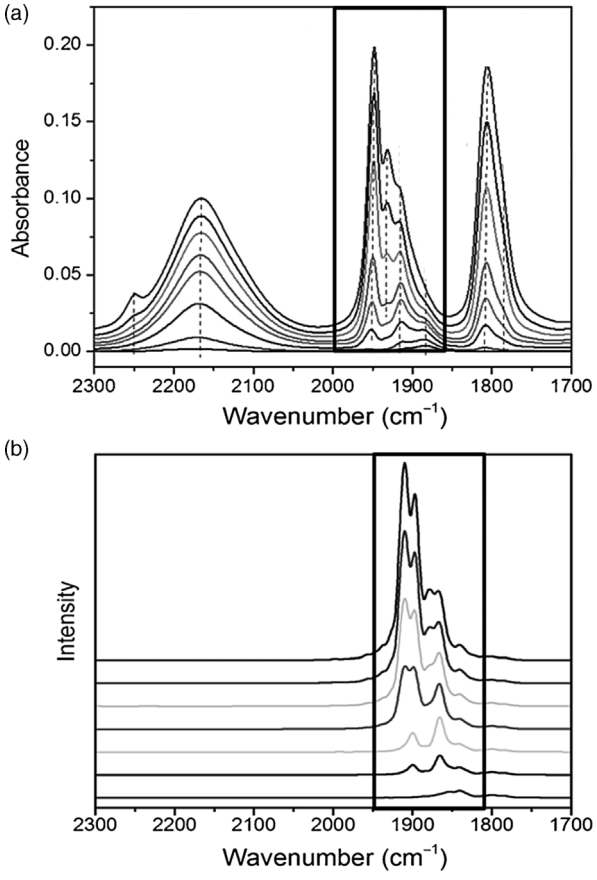

Figure 40.18 (a) Experimental [100] and (b) simulated IR spectrum [99] for different NO loadings adsorbed to copper(II) sites in zeolites. The modeled spectrum is based upon a linear combination of IR spectra corresponding with sites differing in the position of the Al substitution and of the Cu^{II} cation, and the Si/Al ratio. (Reproduced with permission from Ref. [99]. Copyright 2015, Wiley-VCH Verlag GmbH.)

influence on the accuracy of reproduction of low-frequency collective modes [101,102]. To illustrate the accuracy of current force fields we present two applications on MOFs.

In Figure 40.19 the IR-spectrum of HKUST-1 is displayed using the concept of the power spectrum method but with the dipole moment time derivative autocorrelation function instead of the velocity [103]. Overall, even the smaller features of the spectrum above 400 cm^{-1} are well reproduced.

As second example to illustrate the good performance of IR spectra in MOFs nowadays feasible with the current techniques is a VPS spectrum obtained after a NPT MD simulation on a defectless UiO-66 material using a force field constructed for this type of MOF following the concept of QuickFF [104].

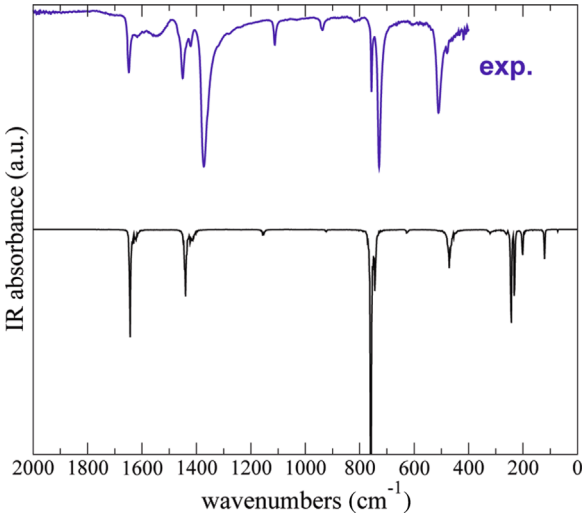

Figure 40.19 Comparison of the computed IR spectrum (bottom) with the measured (top) spectrum for a desolvated, activated Cu-btc (or HKUST-1) sample. (Adapted with permission from Ref. [103]. Copyright 2010, American Chemical Society.)

Experimental information is given by Lillerud and coworkers [55]. Most of the peaks in the experimental IR spectra are well reproduced (see Figure 40.20). The peak around 3675 cm^{-1} belongs to the OH stretch while the CH stretching frequency around 3070 cm^{-1} is not clearly observed in the experimental spectrum: it is very broad with a weak intensity. Here, we can refer to the work of Valenzano *et al.* [105] where weak bands due to the CH stretch are visible. The vibrational frequencies are scaled by a factor of 0.9475, which is a standard procedure to get a better comparison with observed values. The scaling accounts for both systematic errors with force constants and neglected anharmonicities.

A second leading characterization tool in zeolite chemistry (less employed in MOFs) is magic angle spinning (MAS) NMR. Silica zeolites and aluminophosphates (AlPOs) contain NMR-active elements and this makes solid-state NMR as a powerful tool for structure determination. However, in the jungle of peaks in the spectra molecular modeling is an indispensable tool to assist in unraveling the various signals. In contrast to the theoretical reproduction of IR spectra, first-principle calculations are prerequisite here by preference with the help of periodic codes. We refer to a recent review on advances in theory within the field of zeolite chemistry [36] to get an overview of the different periodic codes in which a NMR module has been implemented. Due to the overall complexity of the theoretical procedure only static approaches are suited for computation of NMR chemical shifts, limiting their direct usefulness and future in modus operandi measurements.

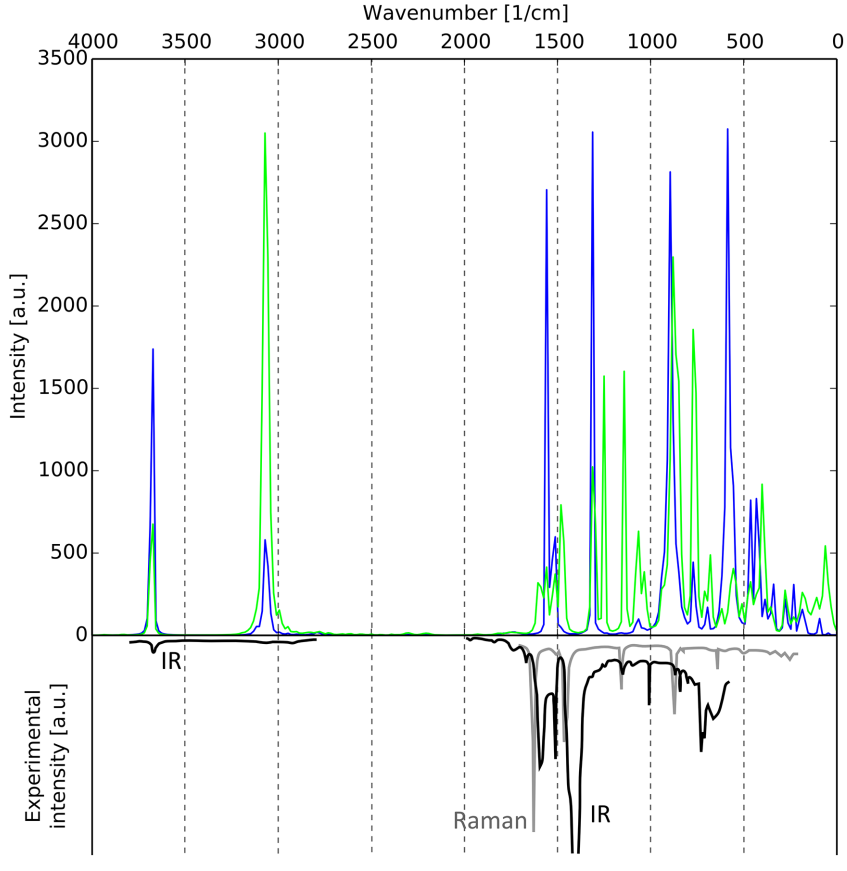

Figure 40.20 Comparison of the computed IR spectrum by means of VPS (green) of a defect free UiO-66 material. The blue spectrum stands for the power spectrum of the change in dipole moment. Experimental FTIR spectra of tagged UiO-66 materials activated at 373 K have been made available by the group of Lillerud [55]. (Reproduced with permission from Ref. [55]. Copyright 2010, American Chemical Society.)

On the other hand, optical spectroscopy has emerged as an ideal technique to study catalyst materials at work, that is, under operando conditions [94]. UV/vis and/or fluorescence spectroscopy can provide information about the single-molecule detection in zeolite-catalyzed reactions [106]. At the same time, the breakthrough of the time-dependent form of DFT, that is, TD-DFT, has also enabled the study of electronic excited states of relatively large systems (up to 400 atoms) [107], making computation of excitation and emission spectra possible with an accuracy of 0.5–0.4 eV. It has opened a lot of perspectives from the theoretical side to give insight in the interpretation of experimental spectra as measured in UV/vis and luminescence

spectroscopy. The technique has evolved to such extent that excited-state properties of large carbonaceous species can be computed, which can be active intermediates in zeolite-catalyzed reactions. They can assist UV/vis experiments combined with confocal fluorescence measurements in identifying hydrocarbon species and their location during the reaction. To illustrate the power of this relatively new characterization technique we present in Figure 40.21 an assignment scale constructed from MD-averaged TD-DFT computations to assign bands in *in situ* UV/vis adsorption spectra to structurally different aromatic HP species. Despite the success of the gas-phase calculations further progress is more than welcome in the theoretical description of the electronically excited state surfaces of real-life systems. To account for the full zeolitic environment further model development is needed to construct the electronic excited state surface using periodic codes, which are routinely used for the description of ground-state properties.

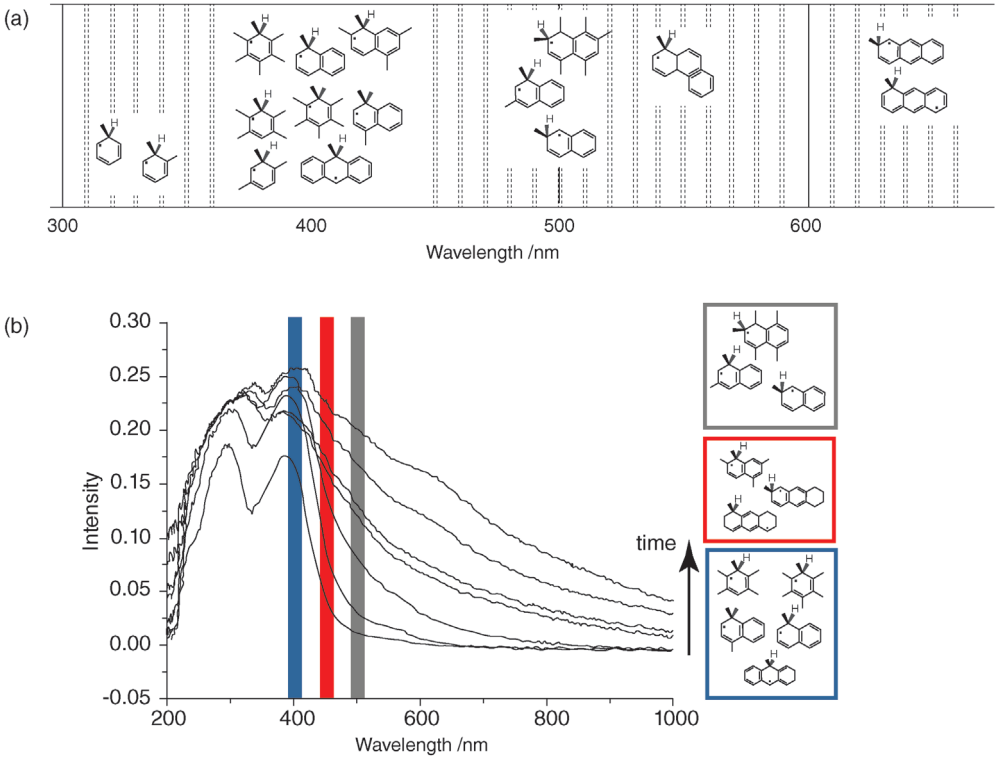

Figure 40.21 Assignment scale constructed from MD-averaged TD-DFT computations (a). Use of the assignment scale to assign bands in *in situ* UV/Vis absorption spectra to structurally different aromatic HP species (b). (Adapted with permission from Ref. [108].)

40.6 Conclusions and Perspectives

With the steady increase of new techniques to model molecular systems and chemical transformations, the expectations are growing equally. The more complexity in the system under study, the more complexity needs to be taken into account in the model. But a model always represents some idealized description of the reality. The more complexity we insert in the model, the better we approach reality. But a phenomenon that exists in nature is governed by so many degrees of freedom, that they can never be taken into account in a model and that a serious and rational selection of external factors has to be done to keep the model as feasible.

Many obstacles have been overcome by molecular modeling, still many challenges are remaining. One of the challenges is the description of phenomena occurring at longer length and time scales and integrating information from various scales toward a unified understanding of the catalyst.

In this paper, we concentrated on the techniques available to model heterogeneous catalysis under reaction conditions, which is of the highest complexity.

Enhanced MD methods have made their entrance within zeolite catalysis and also within chemical transformations in MOFs, but further progress in the methodology is still welcome as existing methods are too biased preventing the exploration of a large part of the free energy surface and neglecting the existence of some realistic pathways.

Appendix A Chemical Kinetics

We report here some established thermodynamic expressions for the convenience of the reader. The molecular partition function Q includes in principle all electronic, translational, rotational, and vibrational motions.

i) Total internal energy:

$$U = \mathrm{RT}^2 \left(\frac{\partial \ln Q}{\partial T} \right)_{\mathrm{N,V}} \tag{40.A.1}$$

decomposed into: $U = U_0 + U_{\mathrm{therm}}$

with $U_0 = E_0 = \varepsilon_0 + E_{\mathrm{ZPE}}$ (ε_0 represents the electronic ground-state energy and $E_{\mathrm{ZPE}} = \sum_{k=1}^{3N-6} \frac{1}{2} h\nu_k$ the zero-point energy), and with the internal thermal energy: $U_{\mathrm{therm}} = U_{\mathrm{trans}} + U_{\mathrm{rot,ext}} + U_{\mathrm{vib}}$.

These thermal contributions can easily be evaluated with the help of Eq. (40.A.1): $U_{\mathrm{trans}} = \frac{3}{2}\mathrm{RT}$; $U_{\mathrm{rot,ext}} = \frac{3}{2}\mathrm{RT}$ (for a nonlinear molecule); $U_{\mathrm{rot,ext}} = \mathrm{RT}$ (for a linear molcule);

$$U_{\mathrm{vib}} = R \sum_{k=1}^{3N-6} \frac{h\nu_k}{k_{\mathrm{B}}} \frac{1}{\mathrm{e}^{\frac{h\nu_k}{k_{\mathrm{B}}T}} - 1}$$

ii) Enthalpy: $H = U + pV$

iii) Entropy:

$$S = R \ln Q + \mathrm{RT}\left(\frac{\partial \ln Q}{\partial T}\right)_{\mathrm{N,V}}$$

iv) (Gibbs) free energy:

$$\begin{aligned} G &= H - \mathrm{TS} \\ &= U_0 + pV - \mathrm{RT} \ln Q \end{aligned}$$

Appendix B Free Energy and Partition Function in Statistical Physics

The free energy of a system of N particles in thermodynamic equilibrium is related to its partition function (in the classical limit)

$$G = -k_{\mathrm{B}} T \ln Z \tag{40.B.1}$$

$$Z = \frac{1}{h^{3N} N!} \int \mathrm{d}\boldsymbol{x}^N \mathrm{d}\boldsymbol{p}^N \mathrm{e}^{-\beta H\left(\boldsymbol{x}^N, \boldsymbol{p}^N\right)} \tag{40.B.2}$$

Suppose, we are interested in the probability distribution as function of a collective variable s, which may be a bond length, an angle, a coordination number, and so on, the partition function can be rewritten in the following form:

$$Z = \int_{-\infty}^{+\infty} Z_{\mathrm{q}}(s) \mathrm{d}s \tag{40.B.3}$$

with

$$Z_{\mathrm{q}}(s) = \frac{1}{h^{3N} N!} \int \mathrm{d}\boldsymbol{x}^N \mathrm{d}\boldsymbol{p}^N \delta\left(Q\left(\boldsymbol{x}^N, \boldsymbol{p}^N\right) - s\right) \mathrm{e}^{-\beta H\left(\boldsymbol{x}^N, \boldsymbol{p}^N\right)} \tag{40.B.4}$$

with $Z_q(s)\,\mathrm{d}s$ the contribution to the total partition function Z due to a microstate with a value of s in the range $[s, s + \mathrm{d}s]$. Furthermore, one can rewrite the equation above in terms of a probability distribution $P_{\mathrm{q}}(s)$

$$P_{\mathrm{q}}(s) = \frac{Z_{\mathrm{q}}(s)}{Z} \quad \text{with the normalization} \quad \int_{-\infty}^{+\infty} P_{\mathrm{q}}(s) \mathrm{d}s = 1.$$

However, if we would associate the free energy of such a microstate as

$$G_{\mathrm{q}}(s) = -k_{\mathrm{B}} T \ln Z_{\mathrm{q}}(s) \tag{40.B.5}$$

– as usual – we immediately notice a dimensionality problem, because $Z_{\mathrm{q}}(s)$ has the dimension of $[\mathrm{s}]^{-1}$. One possible way to resolve this issue is by considering

differences in free energies at two different values of s

$$G_{\mathrm{q}}(s_2) - G_{\mathrm{q}}(s_1) = -k_{\mathrm{B}}T \ln \frac{Z_{\mathrm{q}}(s_2)}{Z_{\mathrm{q}}(s_1)} = -k_{\mathrm{B}}T \ln \frac{P_{\mathrm{q}}(s_2)}{P_{\mathrm{q}}(s_1)} \quad \left(= -k_{\mathrm{B}}T \ln \frac{Z_{\mathrm{q}}(s_2)\mathrm{d}s}{Z_{\mathrm{q}}(s_1)\mathrm{d}s} \right). \tag{40.B.6}$$

The ratio of the probability distributions in the argument of the logarithm defines whether it is more probable to find the system in the range $[s_2, \mathrm{s}_2 + \mathrm{d}s]$ than to find it in the range $[s_1, \mathrm{s}_1 + \mathrm{d}s]$, or vice versa. The ratio $P_{\mathrm{q}}(s_2)/P_{\mathrm{q}}(s_1)$ also defines whether $G_{\mathrm{q}}(s_2) > G_{\mathrm{q}}(s_1)$ or $G_{\mathrm{q}}(s_2) < G_{\mathrm{q}}(s_1)$. This is also exactly how this free energy difference should be interpreted.

Alternatively, one could define a macrostate A for which s lies in the range $[\mathrm{s}_1, s_2]$. This gives rise to the following expressions:

$$Z_{\mathrm{A}} = \int_{s_1}^{s_2} Z_{\mathrm{q}}(s)\mathrm{d}s.$$

$$P_{\mathrm{A}} = \frac{Z_A}{Z}.$$

$$G_{\mathrm{A}} = -k_{\mathrm{B}}T \ln Z_A = -k_{\mathrm{B}}T \ln \frac{Z_{\mathrm{A}}}{Z} - k_{\mathrm{B}}T \ln Z.$$

$$G_{\mathrm{A}} = -k_{\mathrm{B}}T \ln P_{\mathrm{A}} + G.$$

In this case Z_{A}, must be interpreted as the contribution to the partition function from the macrostate A. Similarly, G_{A} can be interpreted as the free energy associated with the macrostate A that can be computed up to a constant G, which is the total free energy. Finally, if we can assume that the partition function has a constant value of $Z_q(\bar{s})$ in that range $[s_1, s_2]$, the equations reduce to

$$Z_{\mathrm{A}} = Z_q(\bar{s})\Delta s.$$

$$P_{\mathrm{A}} = \frac{Z_{\mathrm{q}}(\bar{s})\Delta s}{Z}.$$

$$G_{\mathrm{A}} = -k_{\mathrm{B}}T \ln Z_{\mathrm{q}}(\bar{s})\Delta s.$$

with $\bar{s} = \frac{s_1+s_2}{2}$ and $\Delta s = s_2 - s_1$.

Given this background, we can now define the free energy barrier $\Delta G^{\ddagger}$ based on the one-dimensional free energy profile $G_{\mathrm{q}}(s)$. We define two states: R representative for the reactants, and TS representative for the transition-state region. The choice of these states can be done according to the two approaches outlined above. In the first approach, we identify R with the microstate corresponding to the minimum of $G_{\mathrm{q}}(s)$ in the reactant valley and TS with the microstate corresponding to the maximum of $G_q(s)$. This gives rise to

$$\Delta G^{\ddagger} = G_q(s_{\mathrm{TS}}) - G_{\mathrm{q}}(s_{\mathrm{R}}). \tag{40.B.7}$$

This method entails just taking the free energy difference between the maximum of the free energy profile and the minimum, which yields a very rough estimate of the free energy barrier.

Acknowledgments

The authors acknowledge the Fund for Scientific Research – Flanders (FWO), the Research Board of Ghent University (BOF), BELSPO in the frame of IAP/7/05 and the fund for scientific research Flanders (FWO) for financial support. VVS and KDW acknowledge funding from the European Union's Horizon 2020 Research and Innovation Programme (consolidator ERC grant agreement No 647755 – DYNPOR (2015-2020)). The computational resources and services used in this work were provided by VSC (Flemish Supercomputer Center), funded by the Hercules foundation and the Flemish Government – department EWI.

References

1 Joos, L. *et al.* (2015) Carbon capture turned upside down: high-temperature adsorption & low-temperature desorption (HALD). *Energy Environ. Sci.*, **8** (8), 2480–2491.
2 Kim, J. *et al.* (2012) High-throughput characterization of porous materials using graphics processing units. *J. Chem. Theory Comput.*, **8** (5), 1684–1693.
3 Simon, C.M. *et al.* (2015) The materials genome in action: identifying the performance limits for methane storage. *Energy Environ. Sci.*, **8** (4), 1190–1199.
4 Colon, Y.J. and Snurr, R.Q. (2014) High-throughput computational screening of metal-organic frameworks. *Chem. Soc. Rev.*, **43** (16), 5735–5749.
5 Weckhuysen, B.M. (2009) Chemical imaging of spatial heterogeneities in catalytic solids at different length and time scales. *Angew. Chem., Int. Ed.*, **48** (27), 4910–4943.
6 Piccini, G., Alessio, M., and Sauer, J. (2016) *Ab initio* calculation of rate constants for molecule–surface reactions with chemical accuracy. *Angew. Chem., Int. Ed.*, **55** (17), 5235–5237.
7 Svelle, S. *et al.* (2009) Quantum chemical modeling of zeolite-catalyzed methylation reactions: toward chemical accuracy for barriers. *J. Am. Chem. Soc.*, **131** (2), 816–825.
8 Van Speybroeck, V. *et al.* (2011) First principle kinetic studies of zeolite-catalyzed methylation reactions. *J. Am. Chem. Soc.*, **133** (4), 888–899.
9 Sauer, J. and Freund, H.-J. (2015) Models in catalysis. *Catal. Lett.*, **145** (1), 109–125.
10 De Wispelaere, K., Bailleul, S., and Van Speybroeck, V. (2016) Towards molecular control of elementary reactions in zeolite catalysis by advanced molecular simulations mimicking operating conditions. *Catal. Sci. Tech.*, **6** (8), 2686–2705.
11 De Wispelaere, K. *et al.* (2015) Complex reaction environments and competing reaction mechanisms in zeolite catalysis: insights from advanced molecular dynamics. *Chem. Eur. J.*, **21** (26), 9385–9396.
12 De Wispelaere, K. *et al.* (2016) Insight into the effect of water on the methanol-to-olefins conversion in H-SAPO-34 from molecular simulations and in situ microspectroscopy. *ACS Catal.*, **6**, 1991–2002.

13 Moors, S.L.C. *et al.* (2013) Molecular dynamics kinetic study on the zeolite-catalyzed benzene methylation in ZSM-5. *ACS Catal.*, **3** (11), 2556–2567.

14 Van der Mynsbrugge, J. *et al.* (2014) Insight into the formation and reactivity of framework-bound methoxide species in H-ZSM-5 from static and dynamic molecular simulations. *ChemCatChem*, **6** (7), 1906–1918.

15 Benco, L., Bucko, T., and Hafner, J. (2011) Dehydrogenation of propane over Zn-MOR. Static and dynamic reaction energy diagram. *J. Catal.*, **277** (1), 104–116.

16 Bucko, T. *et al.* (2009) Mechanism of alkane dehydrogenation catalyzed by acidic zeolites: *ab initio* transition path sampling. *J. Chem. Phys.*, **131** (21), 11.

17 Bucko, T. *et al.* (2011) Monomolecular cracking of propane over acidic chabazite: An ab initio molecular dynamics and transition path sampling study. *J. Catal.*, **279** (1), 220–228.

18 Bučko, T. and Hafner, J. (2015) The role of spatial constraints and entropy in the adsorption and transformation of hydrocarbons catalyzed by zeolites. *J. Catal.*, **329** (0), 32–48.

19 Goltl, F. and Hafner, J. (2013) Modelling the adsorption of short alkanes in protonated chabazite: the impact of dispersion forces and temperature. *Microporous Mesoporous Mat.*, **166** (0), 176–184.

20 Jiang, T. *et al.* (2014) Effect of temperature on the adsorption of short alkanes in the zeolite SSZ-13—adapting adsorption isotherms to microporous materials. *ACS Catal.*, **4** (7), 2351–2358.

21 Gomes, J., Head-Gordon, M., and Bell, A.T. (2014) Reaction dynamics of zeolite-catalyzed alkene methylation by methanol. *J. Phys. Chem. C*, **118** (37), 21409–21419.

22 Zimmerman, P.M. *et al.* (2012) *Ab initio* simulations reveal that reaction dynamics strongly affect product selectivity for the cracking of alkanes over H-MFI. *J. Am. Chem. Soc.*, **134** (47), 19468–19476.

23 Van Speybroeck, V. *et al.* (2014) First principle chemical kinetics in zeolites: the methanol-to-olefin process as a case study. *Chem. Soc. Rev.*, **43** (21), 7326–7357.

24 Corma, A. (2003) State of the art and future challenges of zeolites as catalysts. *J. Catal.*, **216** (1–2), 298–312.

25 Rowsell, J.L.C. and Yaghi, O.M. (2004) Metal-organic frameworks: a new class of porous materials. *Microporous Mesoporous Mat.*, **73** (1–2), 3–14.

26 Ferey, G. (2008) Hybrid porous solids: past, present, future. *Chem. Soc. Rev.*, **37** (1), 191–214.

27 Vermoortele, F. *et al.* (2012) Electronic effects of linker substitution on lewis acid catalysis with metal-organic frameworks. *Angew. Chem., Int. Ed.*, **51** (20), 4887–4890.

28 Li, H. *et al.* (1999) Design and synthesis of an exceptionally stable and highly porous metal-organic framework. *Nature*, **402** (6759), 276–279.

29 Maihom, T. *et al.* (2009) Reaction mechanisms of the methylation of ethene with methanol and dimethyl ether over H-ZSM-5: an ONIOM study. *J. Phys. Chem. C*, **113** (16), 6654–6662.

30 Dapprich, S. *et al.* (1999) A new ONIOM implementation in Gaussian98. Part I. The calculation of energies, gradients, vibrational frequencies and electric field derivatives. *J. Mol. Struct. Theochem.*, **461**, 1–21.

31 Bulo, R.E. *et al.* (2009) Toward a practical method for adaptive QM/MM simulations. *J. Chem. Theory Comput.*, **5** (9), 2212–2221.

32 Gomes, J. *et al.* (2012) Accurate prediction of hydrocarbon interactions with zeolites utilizing improved exchange-correlation functionals and QM/MM methods: benchmark calculations of adsorption enthalpies and application to ethene methylation by methanol. *J. Phys. Chem. C*, **116** (29), 15406–15414.

33 Tranca, D.C. *et al.* (2015) Hexane cracking on ZSM-5 and faujasite zeolites: a QM/MM/QCT study. *J. Phys. Chem. C*, **119** (52), 28836–28853.

34 Nieminen, V. *et al.* (2005) Stabilities of C3–C5 alkoxide species inside H-FER zeolite: a hybrid QM/MM study. *J. Catal.*, **231** (2), 393–404.

35 Grimme, S. *et al.* (2010) A consistent and accurate *ab initio* parametrization of density functional dispersion correction (DFT-D) for the 94 elements H-Pu. *J. Chem. Phys.*, **132** (15), 154104.

36 Van Speybroeck, V. *et al.* (2015) Advances in theory and their application within the field of zeolite chemistry. *Chem. Soc. Rev.*, **44** (20), 7044–7111.

37 Notari, B. (1996) Microporous crystalline titanium silicates, in *Advances in Catalysis*, vol **41** (eds D.D. Eley, W.O. Haag, and B. Gates), Elsevier, pp. 253–334.

38 Yarulina, I., Bailleul, S., Pustovarenko, A., Martinez, J.R., Wispelaere, K.D., Hajek, J., Weckhuysen, B.M., Houben, K., Baldus, M., Van Speybroeck, V., Kapteijn, F., and Gascon, J. (2016) Suppression of the aromatic cycle in methanol-to-olefins reaction over ZSM-5 by post-synthetic modification using calcium. *ChemCatChem*, **8**, 3057.

39 Dedecek, J., Kaucky, D., and Wichterlova, B. (2001) Al distribution in ZSM-5 zeolites: an experimental study. *Chem. Commun.*, **2001** (11), 970–971.

40 Sklenak, S. *et al.* (2007) Aluminum siting in silicon-rich zeolite frameworks: a combined high-resolution Al-27 NMR spectroscopy and quantum mechanics/molecular mechanics study of ZSM-5. *Angew. Chem., Int. Ed.*, **46** (38), 7286–7289.

41 Sklenak, S. *et al.* (2009) Aluminium siting in the ZSM-5 framework by combination of high resolution Al-27 NMR and DFT/MM calculations. *Phys. Chem. Chem. Phys.*, **11** (8), 1237–1247.

42 Van der Mynsbrugge, J. *et al.* (2012) Methylation of benzene by methanol: single-site kinetics over H-ZSM-5 and H-beta zeolite catalysts. *J. Catal.*, **292**, 201–212.

43 Van der Mynsbrugge, J. *et al.* (2012) Efficient approach for the computational study of alcohol and nitrile adsorption in H-ZSM-5. *J. Phys. Chem. C*, **116** (9), 5499–5508.

44 Lo, C. *et al.* (2004) Methanol coupling in the zeolite chabazite studied via Car-Parrinello molecular dynamics. *Mol. Phys.*, **102** (3), 281–288.

45 Sauer, J., Sierka, M., and Haase, F. (1999) Acidic catalysis by zeolites. Ab initio modeling of transition structures, in *Transitions State Modeling for Catalysis* (eds K. Morokuma and D.G. Truhlar), American Chemical Society, Washington DC, pp. 358–367.

46 Haase, F., Sauer, J., and Hutter, J. (1997) *Ab initio* molecular dynamics simulation of methanol adsorbed in chabazite. *Chem. Phys. Lett.*, **266** (3–4), 397–402.

47 Stich, I. *et al.* (1999) Role of the zeolitic environment in catalytic activation of methanol. *J. Am. Chem. Soc.*, **121** (14), 3292–3302.

48 Gale, J.D. *et al.* (1999) Methanol in microporous materials from first principles. *Catal. Today*, **50** (3–4), 525–532.

49 Termath, V. *et al.* (1998) Understanding the nature of water bound to solid acid surfaces. *Ab initio* simulation on HSAPO-34. *J. Am. Chem. Soc.*, **120** (33), 8512–8516.

50 Jeanvoine, Y. *et al.* (1998) Bronsted acid sites in HSAPO-34 and chabazite: an *ab initio* structural study. *J. Phys. Chem. B*, **102** (29), 5573–5580.

51 Vener, M.V., Rozanska, X., and Sauer, J. (2009) Protonation of water clusters in the cavities of acidic zeolites: $(H_2O)(n)$ center dot H-chabazite, $n = 1–4$. *Phys. Chem. Chem. Phys.*, **11** (11), 1702–1712.

52 Joshi, K.L. *et al.* (2014) Reactive molecular simulations of protonation of water clusters and depletion of acidity in H-ZSM-5 zeolite. *Phys. Chem. Chem. Phys.*, **16** (34), 18433–18441.

53 Cavka, J.H. *et al.* (2008) A new zirconium inorganic building brick forming metal organic frameworks with exceptional stability. *J. Am. Chem. Soc.*, **130** (42), 13850–13851.

54 Guillerm, V. *et al.* (2010) A zirconium methacrylate oxocluster as precursor for the low-temperature synthesis of porous zirconium(IV) dicarboxylates. *Chem. Commun.*, **46** (5), 767–769.

55 Kandiah, M. *et al.* (2010) Synthesis and stability of tagged UiO-66 Zr-MOFs. *Chem. Mater.*, **22** (24), 6632–6640.

56 Vandichel, M. *et al.* (2015) Active site engineering of UiO-66 type metal-

organic frameworks by intentional creation of defects: a theoretical rationalization. *CrystEngComm*, **17**, 395–406.
57 Hajek, J. *et al.* (2015) Mechanistic studies of aldol condensations in UiO-66 and UiO-66-NH2 metal organic frameworks. *J. Catal.*, **331**, 1–12.
58 Cliffe, M.J. *et al.* (2014) Correlated defect nanoregions in a metal-organic framework. *Nat. Commun.*, **5**, 4176.
59 Oien, S. *et al.* (2014) Detailed structure analysis of atomic positions and defects in zirconium metal-organic frameworks. *Cryst. Growth Des.*, **14** (11), 5370–5372.
60 Trickett, C.A. *et al.* (2015) Definitive molecular level characterization of defects in UiO-66 crystals. *Angew. Chem., Int. Ed.*, **54** (38), 11162–11167.
61 Ling, S. and Slater, B. (2016) Dynamic acidity in defective UiO-66. *Chem. Sci.*, **2016** (7), 4706–4712.
62 Vandichel, M. *et al.* (2016) Water coordination and dehydroxylation processes in defective UiO-66 type metal-organic frameworks. *CrystEngComm*, **18** (37), 7056–7069.
63 Kresse, G. and Furthmuller, J. (1996) Efficient iterative schemes for *ab initio* total-energy calculations using a plane-wave basis set. *Phys. Rev. B*, **54** (16), 11169–11186.
64 Kresse, G. and Furthmüller, J. (1996) Efficiency of *ab initio* total energy calculations for metals and semiconductors using a plane-wave basis set. *Comput. Mat. Sci.*, **6**, 15.
65 Kresse, G. and Hafner, J. (1993) *Ab initio* molecular-dynamics for liquid-metals. *Phys. Rev. B*, **47** (1), 558–561.
66 Kresse, G. and Hafner, J. (1994) *Ab initio* molecular-dynamics simulation of the liquid-metal-amorphous-semiconductor transition in germanium. *Phys. Rev. B*, **49**, 14251.
67 Bhan, A. *et al.* (2003) DFT investigation of alkoxide formation from olefins in H-ZSM-5. *J. Phys. Chem. B*, **107** (38), 10476–10487.
68 Ishikawa, H. *et al.* (1999) Stable dimerized alkoxy species of 2-methylpropene on mordenite zeolite studied by FT-IR. *J. Phys. Chem. B*, **103** (27), 5681–5686.
69 Kondo, J.N. *et al.* (1997) IR study of adsorption and reaction of 1-butene on H-ZSM-5. *Catal. Lett.*, **47** (2), 129–133.
70 Nguyen, C.M. *et al.* (2011) Physisorption and chemisorption of linear alkenes in zeolites: a combined QM-Pot(MP2// B3LYP:GULP)-statistical thermodynamics study. *J. Phys. Chem. C*, **115** (48), 23831–23847.
71 Boronat, M., Viruela, P.M., and Corma, A. (2004) Reaction intermediates in acid catalysis by zeolites: prediction of the relative tendency to form alkoxides or carbocations as a function of hydrocarbon nature and active site structure. *J. Am. Chem. Soc.*, **126** (10), 3300–3309.
72 Kondo, J.N., Wakabayashi, F., and Domen, K. (1998) IR study of adsorption of olefins on deuterated ZSM-5. *J. Phys. Chem. B*, **102** (12), 2259–2262.
73 Frenkel, D. and Smit, B. (2002) *Understanding Molecular Simulations*, 2nd edn, Academic Press, Elsevier.
74 Hajek, J. *et al.* (2016) On the stability and nature of adsorbed pentene in Brønsted acid zeolite H-ZSM-5 at 323 K. *J. Catal.*, **340**, 227–235.
75 Goeltl, F. *et al.* (2012) Van der Waals interactions between hydrocarbon molecules and zeolites: periodic calculations at different levels of theory, from density functional theory to the random phase approximation and Moller-Plesset perturbation theory. *J. Chem. Phys.*, **137** (11), 114111.
76 De Wispelaere, K. *et al.* (2015) Complex reaction environments and competing reaction mechanisms in zeolite catalysis: insights from advanced molecular dynamics. *Chem. Eur. J.*, **21** (26), 9385–9396.
77 Perdew, J.P., Burke, K., and Ernzerhof, M. (1997) Generalized gradient approximation made simple (vol 77, pg 3865 1996). *Phys. Rev. Lett.*, **78** (7), 1396–1396.
78 Yang, K. *et al.* (2010) Tests of the RPBE, revPBE, tau-HCTHhyb, omega B97X-D, and MOHLYP density functional approximations and 29 others against

representative databases for diverse bond energies and barrier heights in catalysis. *J. Chem. Phys.*, **132** (16), 10.
79 Wellendorff, J. *et al.* (2012) Density functionals for surface science: Exchange-correlation model development with Bayesian error estimation. *Phys. Rev. B*, **85** (23), 235149.
80 Ambrosetti, A. *et al.* (2014) Long-range correlation energy calculated from coupled atomic response functions. *J. Chem. Phys.*, **140** (18), 18A508.
81 Bučko, T. *et al.* (2016) Many-body dispersion corrections for periodic systems: an efficient reciprocal space implementation. *J. Phys. Condens. Matter.*, **28** (4), 045201.
82 Aryasetiawan, F., Miyake, T., and Terakura, K. (2002) Total energy method from many-body formulation. *Phys. Rev. Lett.*, **88** (16), 166401.
83 Goltl, F. and Hafner, J. (2011) Alkane adsorption in Na-exchanged chabazite: The influence of dispersion forces. *J. Chem. Phys.*, **134** (6), 064102.
84 Frisch, M.J. *et al.* (2009) *Gaussian 09 {R} evision {A}. 02*, Gaussian, Inc., Wallingford CT.
85 Jones, A.J. and Iglesia, E. (2014) Kinetic, spectroscopic, and theoretical assessment of associative and dissociative methanol dehydration routes in zeolites. *Angew. Chem., Int. Ed.*, **53** (45), 12177–12181.
86 Brogaard, R.Y. *et al.* (2014) Methanol-to-hydrocarbons conversion: the alkene methylation pathway. *J. Catal.*, **314** (0), 159–169.
87 Laio, A. and Gervasio, F.L. (2008) Metadynamics: a method to simulate rare events and reconstruct the free energy in biophysics, chemistry and material science. *Rep. Prog. Phys.*, **71** (12), 22.
88 Laio, A. and Parrinello, M. (2002) Escaping free-energy minima. *Proc. Natl. Acad. Sci. USA*, **99** (20), 12562–12566.
89 Bolhuis, P.G. *et al.* (2002) Transition path sampling: throwing ropes over rough mountain passes, in the dark. *Annu. Rev. Phys. Chem.*, **53**, 291–318.
90 Dellago, C., Bolhuis, P.G., and Geissler, P.L. (2002) Transition path sampling. *Adv. Chem. Phys.*, Vol 123, **123**, 1–78.
91 Bucko, T. *et al.* (2009) Mechanism of alkane dehydrogenation catalyzed by acidic zeolites: Ab initio transition path sampling. *J. Chem. Phys.*, **131** (21), 214508.
92 Ensing, B. (2013) Chemistry in Water, First Principles Computer Simulations. Ph.D. thesis, Vrije Universiteit Amsterdam.
93 Ensing, B. *et al.* (2005) A recipe for the computation of the free energy barrier and the lowest free energy path of concerted reactions. *J. Phys. Chem. B*, **109** (14), 6676–6687.
94 Weckhuysen, B.M. (2010) Preface: recent advances in the *in situ* characterization of heterogeneous catalysts. *Chem. Soc. Rev.*, **39** (12), 4557–4559.
95 Silaghi, M.-C. *et al.* (2016) Dealumination mechanisms of zeolites and extra-framework aluminum confinement. *J. Catal.*, **339**, 242–255.
96 Brogaard, R.Y., Weckhuysen, B.M., and Norskov, J.K. (2013) Guest–host interactions of arenes in H-ZSM-5 and their impact on methanol-to-hydrocarbons deactivation processes. *J. Catal.*, **300**, 235–241.
97 Piccini, G. and Sauer, J. (2014) Effect of anharmonicity on adsorption thermodynamics. *J. Chem. Theory Comput.*, **10** (6), 2479–2487.
98 Bornhauser, P. and Bougeard, D. (2001) Intensities of the vibrational spectra of siliceous zeolites by molecular dynamics calculations. I. Infrared spectra. *J. Phys. Chem. B*, **105** (1), 36–41.
99 Göltl, F., Sautet, P., and Hermans, I. (2015) Can dynamics be responsible for the complex multipeak infrared spectra of NO adsorbed to copper(II) sites in zeolites? *Angew. Chem., Int. Ed.*, **54** (27), 7799–7804.
100 Zhang, R. *et al.* (2014) NO chemisorption on Cu/SSZ-13: a comparative study from infrared spectroscopy and DFT calculations. *ACS Catal.*, **4** (11), 4093–4105.
101 Bueno-Perez, R. *et al.* (2012) Zeolite force fields and experimental siliceous frameworks in a comparative infrared study. *J. Phys. Chem. C*, **116** (49), 25797–25805.

102 Maurin, G. *et al.* (2004) Theoretical prediction of low-frequency vibrations of extra-framework cations in mordenite zeolites. *Phys. Chem. Chem. Phys.*, **6** (1), 182–187.

103 Tafipolsky, M., Amirjalayer, S., and Schmid, R. (2010) First-principles-derived force field for copper paddle-wheel-based metal-organic frameworks. *J. Phys. Chem. C*, **114** (34), 14402–14409.

104 Vanduyfhuys, L. *et al.* (2015) QuickFF: a program for a quick and easy derivation of force fields for metal-organic frameworks from *ab initio* input. *J. Comput. Chem.*, **36** (13), 1015–1027.

105 Valenzano, L. *et al.* (2011) Disclosing the complex structure of UiO-66 metal organic framework: a synergic combination of experiment and theory. *Chem. Mater.*, **23** (7), 1700–1718.

106 Janssen, K.P.F. *et al.* (2014) Single molecule methods for the study of catalysis: from enzymes to heterogeneous catalysts. *Chem. Soc. Rev.*, **43** (4), 990–1006.

107 Adamo, C. and Jacquemin, D. (2013) The calculations of excited-state properties with time-dependent density functional theory. *Chem. Soc. Rev.*, **42** (3), 845–856.

108 Hemelsoet, K. *et al.* (2013) Identification of intermediates in zeolite-catalyzed reactions by *in situ* UV/Vis microspectroscopy and a complementary set of molecular simulations. *Chem. Eur. J.*, **19** (49), 16595–16606.